

Segmentation of Abdominal Adipose Tissue in MRI in a Clinical Study of Growth and Diet

Josephine Jensen and Cecilie Benedicte Anker

Kongens Lyngby 2011

Technical University of Denmark
Informatics and Mathematical Modelling
Building 321, DK-2800 Kongens Lyngby, Denmark
Phone +45 45253351, Fax +45 45882673
reception@imm.dtu.dk
www.imm.dtu.dk

Abstract

This thesis describes *Graph Cut* as a method applied for automatic segmentation of boundaries using information in three dimensions from T1-weighted 3-dimensional abdominal Magnetic Resonance Images, MRI. The data origins from a clinical research study where the subjects are scanned prior to and after 12 weeks of intervention.

The abdomen boundary, interior SAT boundary and Scarpa's Fascia divide the abdomen into three compartments containing different adipose tissue classes. The classes are called visceral adipose tissue, VAT, deep subcutaneous adipose tissue, dSAT, and superficial subcutaneous adipose tissue, sSAT. Research shows different clinical relevance of the three classes.

Before the segmentation the MRI data are preprocessed in several steps. The spatial image intensity inhomogeneities, called the *Bias Field*, are removed. Two methods, a *Thin Plate Spline* and *N3*, for correcting the bias field effect are investigated before choosing which to apply.

The interior SAT boundary and Scarpa's Fascia are located using *Graph Cuts*. A weighted directed graph is constructed from image characteristics. A *Maximum Flow / Minimum Cut* algorithm cuts the graph by finding the maximum flow. For labeling the adipose and nonadipose tissue two methods are compared, *Fuzzy C-Means Clustering* and *Graph Cut*.

A statistical analysis is performed on weight losses according to the intervention groups. Furthermore, the segmentation method described in this thesis is statistically compared to a previous method.

Resumé

Denne afhandling beskriver, hvordan *Graph Cuts* anvendes som en metode til automatisk segmentering af afgrænsninger i maveregionen ved brug af information i tre dimensioner fra T1-vægtet, tredimensionelle Magnetisk Resonans billeder, MR. Datasættet stammer fra et klinisk forskningsstudie, hvor forsøgspersonerne er blevet skannet før og efter 12 ugers intervention.

Den abdominale afgrænsning, den interiore SAT afgrænsning og Scarpas Fascia opdeler maveregionen i tre rum, der indeholder forskellige fedtvævs klasser. Klasserne kaldes visceralt fedtvæv, VAT, dybt subkutant fedtvæv, dSAT, og overfladisk subkutant fedtvæv, sSAT. Forskning viser, at de tre klasser har forskellig klinisk relevans.

Før segmenteringen skal MR data forarbejdes i flere trin. De spatiale billedintensitets inhomogeniteter, som kaldes *Bias Feltet* skal fjernes. To metoder, *Thin Plate Spline* og *N3*, til at korrigere bias feltet er undersøgt, før der vælges, hvilken der benyttes.

Den interiore SAT afgrænsning og Scarpas Fascia er lokaliseret vha. *Graph Cuts*. En retningsbestemt, vægtet graf konstrueres ud fra billedegenskaber. En *Maximum Flow / Minimum Cut* algoritme ”skærer” grafen ved at finde det største *flow*. Til at afmærke hvad der er fedt og ikke-fedt sammenlignes to metoder, *Fuzzy C-means Clustering* og *Graph Cut*.

En statistisk analyse foretages for at sammenligne væggtab med interventionsgrupperne. Ydermere sammenlignes segmenteringsmetoden beskrevet i denne afhandling med en tidligere metode.

Preface

This thesis was prepared at the Department of Informatics Mathematical Modelling (IMM), at the Technical University of Denmark (DTU) in partial fulfillment of the requirements for acquiring the Bachelor of Science degree in engineering, B.Sc.Eng. The undersigned are students in Medicine & Technology at the Technical University of Denmark and the Faculty of Health Sciences, University of Copenhagen. The thesis was supervised by Professor Rasmus Larsen and Professor Knut Conradsen, IMM. The work was carried out from February to June 2011, corresponding to 20 ETCS credits.

Kongens Lyngby, June 2011

Josephine Jensen
&
Cecilie Benedicte Anker

Acknowledgements

We would like to thank the supervisors Professor Rasmus Larsen and Professor Knut Conradsen for expert supervision during the weekly Friday meetings or whenever their expertise were needed during the project.

We thank Thomas Hammershaimb Mosbech, IMM, for lending us the source code from his master thesis project.

We also thank Martin Bæk Petersen, pregraduate research student in medicine at the FINE project, KU, for providing us with the relevant data and information about the intervention study. Associate Professor Bente Merete Stallknecht, KU, is thanked for showing interest in our work and providing relevant literature about the clinical background.

For the help with $N3$ in *Freesurfer*, we thank Mark Lyksborg, IMM, for kind assistance in getting the program running on Mac computers. Furthermore, we thank Jacob Lercke Skytte, IMM, for helping us get the *Maximum Flow / Minimum Cut* algorithm work on Mac computers.

Finally, a very special thank goes to Jacob Schack Vestergaard, IMM, for the nice chats we had in the project room.

Contents

Abstract	i
Resumé	iii
Preface	v
Acknowledgements	vii
1 Introduction	1
1.1 Clinical background	2
1.2 Project goal	5
1.3 Thesis overview	5
2 Data	7
2.1 Image anatomy	8
2.2 Image quality	9
3 Preprocessing	11
3.1 Bias Field	11
3.2 Entropy	15
3.3 Evaluation	19
4 Locating boundaries using Graph Cuts	23
4.1 Graph theory	25
4.2 Graph Cuts	25
4.3 Graph Construction	29
4.4 Evaluation	35

5	Segmenting regions	39
5.1	Identifying Adipose Tissue	39
5.2	Evaluation	44
5.3	Segmenting regions	47
6	Final results	51
6.1	Segmentation results	51
6.2	Statistical analysis	53
6.3	Evaluation	60
7	Conclusion	67
7.1	Future work	68
A	Volume results	69
A.1	Percentage of adipose tissue classes	70
A.2	Percentage weight loss	70
B	Segmentation results	71
C	Software overview	85
D	Data CD	87
E	MATLAB code	89
E.1	M-files	89
F	Statistical analysis in R	97
F.1	R-code	97

CHAPTER 1

Introduction

The prevalence of obesity and overweight in the western world is dramatically increased over the past years and WHO now consider this an epidemic. Obesity is related to the risk of developing diseases as non-insulin-dependent diabetes mellitus (NIDDM), hypertension, and cardiovascular disease. Research in the abdominal adipose tissue field have proposed that an increased amount of visceral adipose tissue, VAT, leads to these metabolic disturbances. Despite this knowledge, investigators doubt that VAT alone is responsible for these risks related to obesity. The abdominal subcutaneous adipose tissue, SAT, may also contribute to these risks [21]. A study by Enevoldsen et al. [7] showed that the break down of lipides is at a lower level in the deep SAT than in the superficial SAT. Likewise, a study has shown a correlation between the amount of deep SAT and insulin resistance. Such a correlation for superficial SAT is not documented. This suggests that the deep SAT has a greater impact on the hormonal balance and thereby the decreased or terminated production of insulin in the endocrine part of pancreas [9]. The development of an automatic method to estimate the depots of VAT, dSAT and sSAT in vivo could on this basis be relevant. A clinical intervention study at the Faculty of Health Sciences at the University of Copenhagen is examining the effect of training due to fat losses of the above-mentioned adipose tissue depots. The MRI data being processed in this thesis origins from this study.

1.1 Clinical background

The increasing obesity is partly explained by changes in lifestyle during the past 60 years, as non-physical sedentary work, less exercise and an overconsumption of food. However, some of the risks of getting one of the lifestyle-related diseases cannot only be explained from lifestyle differences, genetic factors also have an influence. Research show that physical activity has an impact on these factors. The question is, how much exercise a person should do before reducing the risks? It is suggested by the National Health Administration of Denmark, to do 30 minutes of physical activity each day. One of the goals of the clinical study is to determine whether or not the recommendation should be changed in the future.

The clinical intervention study, called *FINE*, has its focus on the effects of physical training on overweight individuals and its related diseases. It is the goal to find the factors, which determine a persons inborn insulin sensitivity, and how physical training influences this and different other metabolic health parameters. The *FINE* (*Four-IN-one*) project has 4 subprojects:

1. Genetic conditional dispersion in the populations' insulin sensitivity.
2. Dose response effects of physical training.
3. Physical training and energy balance.
4. Cultural barrier of physical training.

There are 60 subjects in the study. They are all healthy inactive males between 20 and 40 years and moderate overweight with a Body-Mass-Index, BMI, of 25-30. The subjects are split into 3 groups with different training doses prescribed for 12 weeks. The three intensity groups are: high intensity training (600 kcal/day \sim 1 h), moderate intensity training (300 kcal/day \sim 1/2 h) and a sedentary control group. No restrictions on calorie intake are prescribed. A lot of tests and measurements will be done including MRI scans before and after the 12 weeks' training period [12]. An automatic method to estimate the abdominal adipose tissue depots from the MRI is therefore needed for a comparison with the other clinical data obtained.

VAT is the intraabdominal adipose tissue closest to the organs. VAT surrounds the organs and is commonly thought of, as the adipose tissue of the highest risk related to metabolic diseases. The SAT layer is located just below the skin, and is delimited by the abdomen boundary and the interior SAT boundary. The

SAT layer can be subdivided in a deep and superficial layer, by a thin layer of connective tissue called Scarpa's Fascia. In Figure 1.1 a cross-section of the abdomen is shown. A cross-section of the abdomen is from now on denoted a slice. The dotted red line indicates where Scarpa's Fascia is located. In vivo the fascia is a more smooth boundary.

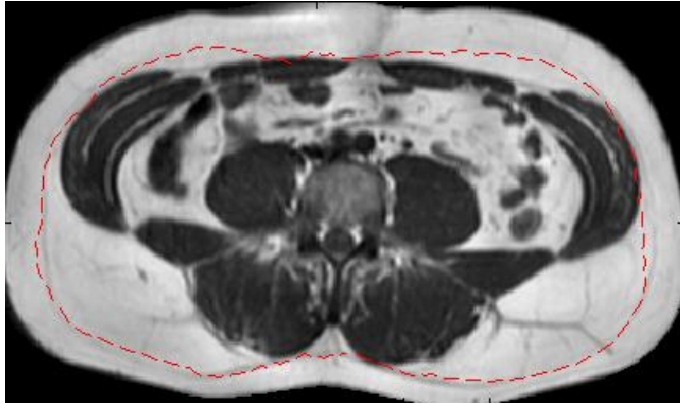
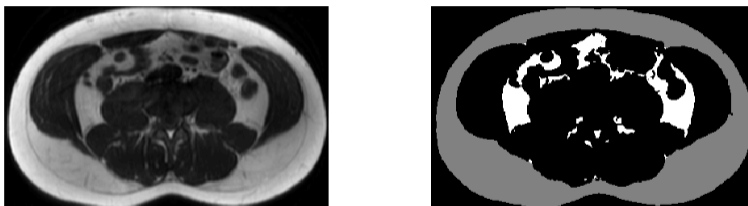


Figure 1.1: Cross-section of the abdomen. The red curve indicates the position of Scarpa's Fascia.

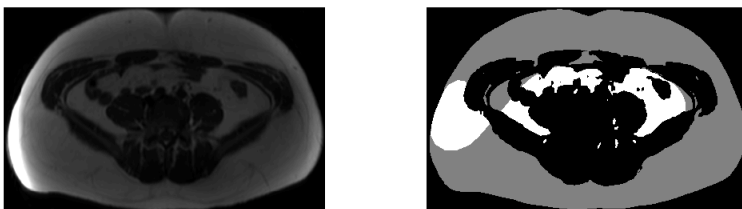
1.1.1 Previous work

It is possible to automatically determine the quantity of VAT, sSAT and dSAT from T1-weighted 3-dimensional MRI data. This can be done by an algorithm developed by Thomas Mosbech, IMM, DTU [18]. The method is from this point called the *Old Method*. The method distinguishes between VAT, sSAT and dSAT. The present MRI data have prior to this project been segmented with this method. This leads to an opportunity of comparison. The method is implemented in 2D, the segmentation is done slice by slice, causing problems related to the segmentation of the adipose tissue classes. Figure 1.2 shows 3 different slices of the abdomen before and after the current program has been run on the MRI data. Figure 1.2 (a) right shows the division of SAT and VAT. It is revealed that the segmentation, at a glance, is well performed. Likewise, Figure 1.2 (b) right shows a division into SAT and VAT. However, the segmentation is not satisfying. A white area, normally indicating VAT, is located in the SAT-area. This is due to the fact that the old method has some difficulties segmenting the boundary between the SAT and VAT layer. Figure 1.2 (c) right shows a division into VAT, dSAT and sSAT. The dSAT and sSAT is segmented by locating Scarpa's Fascia, but as the image reveals, this segmentation is not

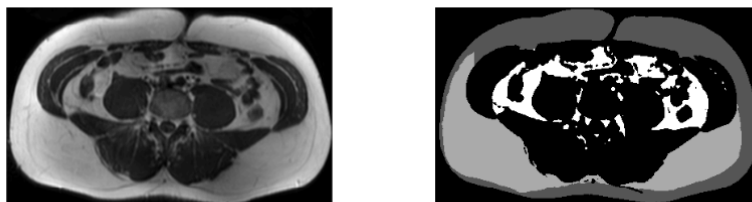
done perfectly, as Scarpa's Fascia is also visible in the upper part. This causes a wrong distribution of sSAT and dSAT. Therefore, the data segmented with the old method is only divided with respect to SAT and VAT. To be able to segment the adipose tissue into dSAT and sSAT it is necessary to locate Scarpa's Fascia more correctly.



(a) Left: MRI of subject 5 slice 6. Right: Segmentation of the left image divided into SAT and VAT.



(b) Left: MRI of subject 47, slice 1. Right: Segmentation of the left image divided into SAT and VAT.



(c) Left: MRI of subject 6, slice 3. Right: Segmentation of the left image divided into dSAT, sSAT and VAT.

Figure 1.2: Different outputs with the current 2D program.

1.2 Project goal

The goal of this thesis is to develop a new method using information in 3 dimensions to determine the distribution of VAT, sSAT and dSAT automatically, from T1-weighted 3-dimensional MRI data. The idea is to transfer information in one slice to its neighbours for a more precise segmentation.

The problem is approached by investigating the slice-by-slice algorithm developed by Thomas Mosbech. A bias field correction using a *Thin Plate Spline* method is already implemented in this program and the task is to improve and compare it to another bias field correction available, called *N3*. The image elements need to be labelled into adipose and non-adipose tissue. Two methods available are compared, *Fuzzy C-means Clustering* and *Graph Cut*. To make it possible to divide the adipose tissue in the abdomen into the relevant tissue types, it is necessary to locate the abdomen boundary, the interior SAT boundary and Scarpa's Fascia. Li et al. [16] present a method called *Graph Cut* for optimal boundary search by initially constructing a weighted directed graph of the 3D dataset. This method is believed to solve the segmentation problem more precisely than the old method.

1.3 Thesis overview

The following section gives a brief overview of the chapters and appendices in the thesis. After chapter 3,4,5 and 6 an evaluation is performed on the intermediate results.

- **Chapter 2 - Data** introduces the data in this project. The image anatomy is described and a comment is made on the image quality.
- **Chapter 3 - Preprocessing** describes how the bias field effect is estimated and removed using two different methods.
- **Chapter 4 - Locating boundaries using Graph Cuts** presents the theory, method and algorithm used for locating the boundaries dividing the abdomen into the relevant adipose tissue compartments.
- **Chapter 5 - Segmenting regions** covers two methods used for labeling the data into adipose and non-adipose tissue. This labeling is combined with the segmented boundaries resulting in the final segmentation.

- **Chapter 6 - Final results** evaluates the segmentation results. A statistical analysis is performed. The results of the analysis are visually compared to the segmentation results. The new and old method are compared as well.
- **Chapter 7 - Conclusion** gives the conclusion together with the future work.
- **Appendix A** holds a table with the final segmentation of 12 subjects together with their weight losses.
- **Appendix B** shows 3 slices of the final segmentation results from 12 subjects.
- **Appendix C** is an overview of the software used in the final segmentation.
- **Appendix D** holds a CD with the original and segmented images obtained by the new and the old method. Voxel percentages of the adipose tissue classes are included together with the algorithm used to get the segmentation results and the R-code.
- **Appendix E** contains important m-files used when *Graph Cutting*.
- **Appendix F** holds the R-code for the statistical analysis.

The dataset consists of 3-dimensional T1-weighted 3 Tesla MRI-scans containing 75 scans. All MRI examinations were done on a 3T Phillips Achieva scanner system (Phillips Medical Systems, Netherlands) at the hospital of Glostrup, Denmark. The coil used was a 16 element phased array coil, with the subjects in the supine position. The images were obtained using a turbo spin echo sequence (36 slices, 7mm thickness, 1mm interslice distance, TR = 500 ms, TE = 15ms, flip angle 90 degrees) [19]. No multi-modal image data is available. Each scan is stored in the DICOM format as a series of slices. A header of data, the *seriesInfo*, reveals the subject's name among other information, such as gender, age and weight. In the *seriesInfo* it is also possible to get information about the image such as modality and size. The header reveals that the resolution of each slice is 512 x 512 pixels. In this thesis the pixels of image slices will be denoted *voxels*, since the data allow them to be regarded as 3-dimensional volume elements.

Each person is scanned twice, prior to the intervention period and at the end. Unfortunately, some of the persons dropped out, which means that no post scanning exists. To be able to do a statistical analysis of the amount of adipose tissue lost or gained only persons with a pre and a post scanning are examined. This is the case for 28 persons. However, for one of the persons 2 post scans exist. Therefore, 57 scans have to be segmented. Each scan is denoted *subject*. An ID-log exists, containing information about which two subjects, make up

one person. The ID-log also reveals the correlation between the persons and the training intensity group. The ID-log will be considered after the segmentation when the statistical analysis is done. Since the clinical study is ongoing, the goal is to apply the developed segmentation method to the rest of the data, which corresponds to about 60 extra subjects.

Since the data is T1-weighted MRI, high image intensities corresponds to adipose tissue, whereas air and tissue with high water content exhibit low image intensity. When displaying the images a method, scaling the intensities to utilize the full colormap, is used. Thus, the displayed intensities are relative and should not be compared between slices.

2.1 Image anatomy

The 3-dimensional data visualizes the abdomen of the given subject, Figure 2.1. There are 36 slices in the image series, but only between 16 and 26 in the middle have to be segmented. The slices of interest, delimited by the L11-L12 disc and the L4-L5 disc, have been selected by a physician in the FINE project at the Faculty of Health Sciences [19]. The same number of slices are selected from the pre and the post scanning.

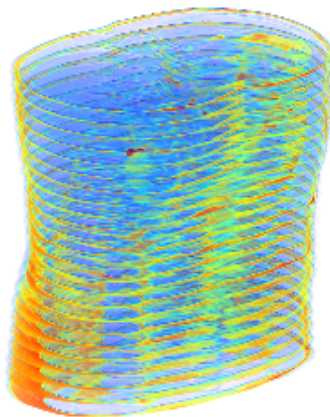


Figure 2.1: 3D plot of the slices of interest in subject 2.

The anterior and posterior part of the images are indicated by a red and a blue arrow respectively in Figure 2.2. Low slice number corresponds to the lower part of the abdomen whereas a high slice number corresponds to the upper part. Organs and structures anatomically located in the right side appear in the left side on the images and vice versa.

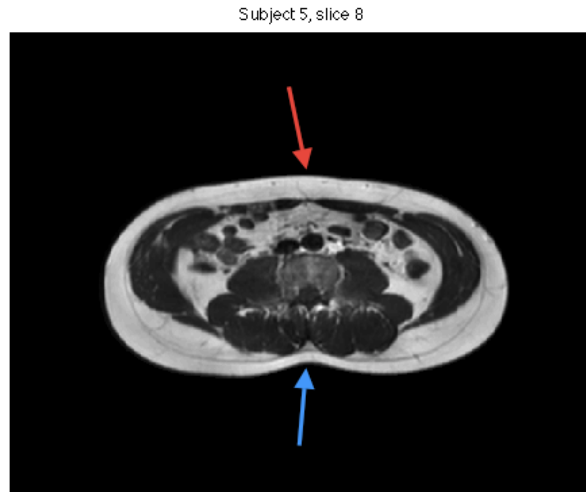


Figure 2.2: Subject 5 slice 8. The red arrow indicates the anterior part of the abdomen, while the blue indicates the posterior part.

2.2 Image quality

Since the data origins from a 3 T MRI scanner with resolution 512x512 the image quality should be considered to be of high quality. However, a rather large number of slices are dark and some have artifacts. There has been doubt about whether or not this is due to an error in the coil. This cannot be confirmed by Glostrup Hospital. An example of a dark slice with artifacts is shown in Figure 2.3.

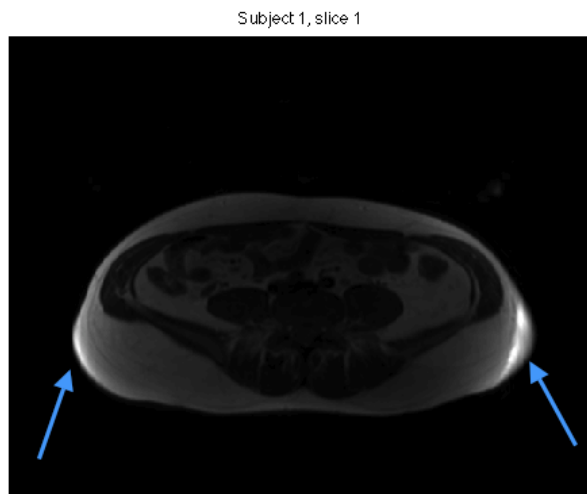


Figure 2.3: Subject 1 slice 1. Dark slice with artifacts indicated by blue arrows.

Preprocessing

3.1 Bias Field

Spatial intensity inhomogeneity is a problem in computer analysis of MRI data because automatic computer segmentation often requires intra-class homogeneity. This inhomogeneity is called the *Bias Field effect*, caused by the radio-frequency coil creating the large magnetic field in the scanner. The subject's anatomy and movements during the scanning can also contribute to the bias field. These parameters make the bias field unique for each subject and scan. The inhomogeneities make it difficult to label the voxels with a tissue type in an automatic and robust way because same-tissue classes have different intensities [2]. Likewise, a phenomenon called *Bias Peaks* is observed in most MRI data due to a sudden change in intensity. The bias field effect in slice 7 of subject 20 is shown in Figure 3.1. The estimation of the bias field is a complicated process and can be done in many ways. In this thesis two methods of estimating the Bias Field effect have been examined before choosing which method is most appropriate for this particular dataset. The methods are called *Thin Plate Spline*, implemented in the old method, and *N3* contained in *Freesurfer*.

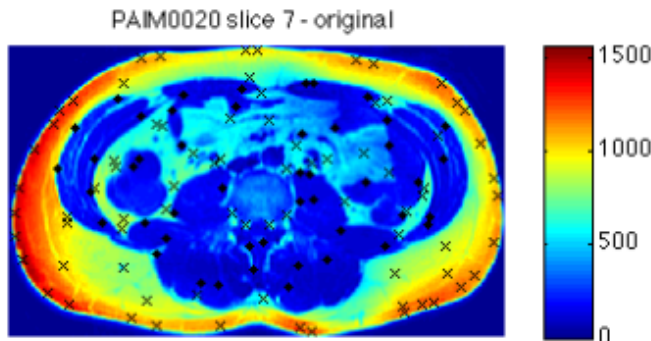


Figure 3.1: Slice 7 of subject 20, showing the bias field effect before a correction has been made. The crosses mark the adipose tissue and the dots mark the non-adipose tissue.

3.1.1 Bias Field correction using a *Thin plate spline*

The first step is to locate the abdomen boundary. The abdomen boundary is characterized by a large intensity gradient between the low intensity background and the high intensity skin and SAT-layer. The boundary is located using the method *Active Contours*. When the abdomen boundary is found, the area of interest is extracted from the image and the local maxima and minima inside the abdomen are found. This is done on each slice separately. Local minima indicate high water content points, which characterize non-adipose tissue, while local maxima correspond to adipose tissue points, Figure 3.1. Due to the intensity variation and peaks some of the points will not be positioned correctly. Only correct points must be left in the area of interest, therefore it is necessary to trim the area. This is done by removing local extrema with intensities below a given threshold. Correct points are obtained by subdividing the image into smaller rectangles and only selecting local maxima and minima compared to the other points of the class inside the given region. It is the assumption that the effect of the bias field is almost constant inside every rectangle. The image is divided into 12 subdivisions vertical and 9 subdivisions horizontal with overlaps of 10 voxels vertical and horizontal. The parameters can be varied and have to be chosen carefully. If the rectangles are too large, the assumption of constant bias field is not obtained. On the other hand, the rectangles must not be too small because at least one correct voxel point of each class should be present in each rectangle. In each rectangle, points, which do not have an intensity over a given threshold relative to the local maxima or minima, respectively, are

discarded.

The first step in the estimation of the true image is to logarithmically transform the points found in the previous step by the following equation.

$$\log(y_{observed}) = \log(y_{true}) + \log(y_{bias}) \Leftrightarrow \quad (3.1)$$

$$\log(y_{true}) = \log(y_{observed}) - \log(y_{bias}) \quad (3.2)$$

The next step in estimating the bias field is done for the entire 3D volume. When the bias field is known it can be subtracted from the observed points resulting in the true image. A *thin plate spline* model (TPS) is used when estimating a function corresponding to the bias field. This is done from the two classes of points found earlier. The principle is to fit an interpolating TPS to the two point classes. This can be thought of, as an infinite thin metal plate being forced through the points - creating an interpolating fit with minimal bending energy.

Figure 3.2 shows an image intensity histogram before and after the TPS correction is applied. The right figure shows a clear separation of the two intensity peaks compared to the left. Low intensities correspond to non-adipose tissue and high intensities correspond to adipose tissue.

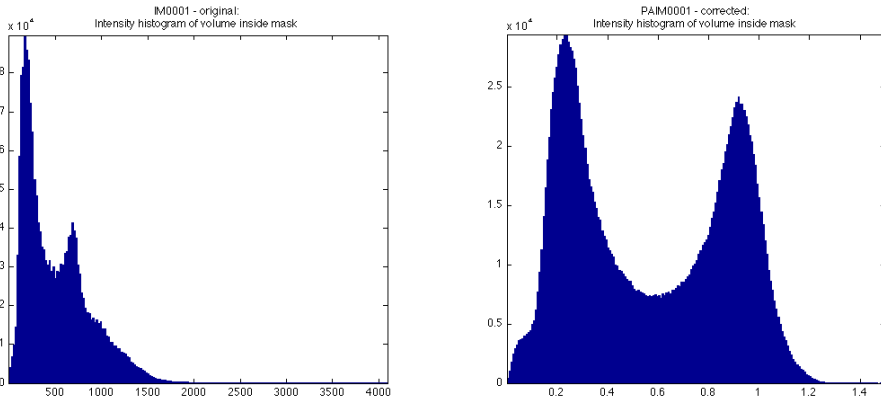


Figure 3.2: Histograms of subject 1 before and after bias field correction with TPS. In the right image the division of the two classes are shown. The left peak corresponds to non-adipose tissue while the right peak is adipose tissue.

In the smoothing TPS function, a parameter alpha, α , controls the amount of smoothness enforced. A low α value will allow the function to have much curva-

ture while a large value will allow less curvature. It is important to determine a value which allows the surface to be flexible, but it must not be too large since this could increase the risk of incorporating noise. There is an optimal value for each subject. However, it is undesirable to select a new and different value of smoothness for each subject and therefore another way of representing this factor is implemented: The *effective degrees of freedom*, df . df can be interpreted as the effective dimensionality of the fit. The purpose is to find a value of the df suitable for all images in the dataset [18], [17]. An investigation to choose the most suitable df is given later in Section [3.2.1].

3.1.2 Bias Field correction with N3 in Freesurfer

The *Freesurfer* program package [13] contains a bias field correction based on the N3 method, a short for nonparametric, nonuniform intensity and normalization algorithm. The method is developed to correct intensity inhomogeneities in brains, where 3 classes of tissue need to be distinguished, grey matter, white matter and cerebrospinal fluid (CSF). The N3 method is based on the following model:

$$v(x) = u(x)f(x) + n(x) \quad (3.3)$$

Where x is the location, v is the measured signal, u is the true signal, f is an unknown smoothly varying bias field over the region of interest (ROI), and n is white noise. The purpose of the correction is to estimate f , however this is difficult using the above equation and a noise-free additive model is used instead, with the notation $\hat{u}(x) = \log[u(x)]$:

$$\hat{v}(x) = \hat{u}(x) + \hat{f}(x) \quad (3.4)$$

The probability densities of \hat{u} , \hat{v} and \hat{f} are U, V and F . If it is assumed, that \hat{u} and \hat{f} are independent random variables, the distribution of their sum is found by convolution:

$$V(\hat{v}) = F(\hat{v}) \otimes U(\hat{v}) = \int F(\hat{v} - \hat{f})U(\hat{f})d\hat{f} \quad (3.5)$$

The task of the N3 correction method is to restore the frequency content of U . Unfortunately, it is not known which frequency components of U that need to

be restored. The field \hat{f} is assumed to be smooth and slowly varying. The N3 approach is to find the smooth slowly varying field that maximizes the frequency content of U. This is done by sharpening the distribution of V, which leads to a suggestion for the distribution of U. The next step is to estimate a smooth field which produces a distribution of U close to the one suggested. It is supposed that the distribution of F is gaussian having zero mean and a given variance, which means that it is only necessary to search for distributions U corresponding to the properties of F. There are different parameters which reflect the result and can be varied. One is the FWHM of F, short for full width at half maximum, which expresses the deconvolution size. Another is the distance, d, which is the distance between basis functions and expresses the smoothness of the estimated field. The size of FWHM has an impact on the convergence rate and performance. A decrease in FWHM would lead to an improvement in accuracy but a decrease in convergence rate, which means a longer computation time. The standard values of FWHM is 0.15 and the distance, d, is 200 mm [20].

3.2 Entropy

The *Shannon entropy* is a measure of the average information content that is missing when the value of the random variable is unknown and therefore the *Shannon entropy* should be as small as possible. The unit is bits and is expressed as:

$$H = - \sum_u (p(u) \cdot \log(p(u))) \quad (3.6)$$

where \log_2 is used. $p(u)$, the probability distribution function, can be calculated from $h(u)$, the image histogram, and N, the sum of the image histogram values, by this formula [15]:

$$p(u) = h(u)/N \quad (3.7)$$

3.2.1 TPS - Effective degrees of freedom

The *Shannon entropies* of four randomly chosen subjects have been calculated for different degrees of freedom, df. A plot of entropy versus df is made for

every subject. This is done to find the most appropriate df to apply on all the subjects. The df chosen should be the most common minimum of all the graphs in Figure 3.3.

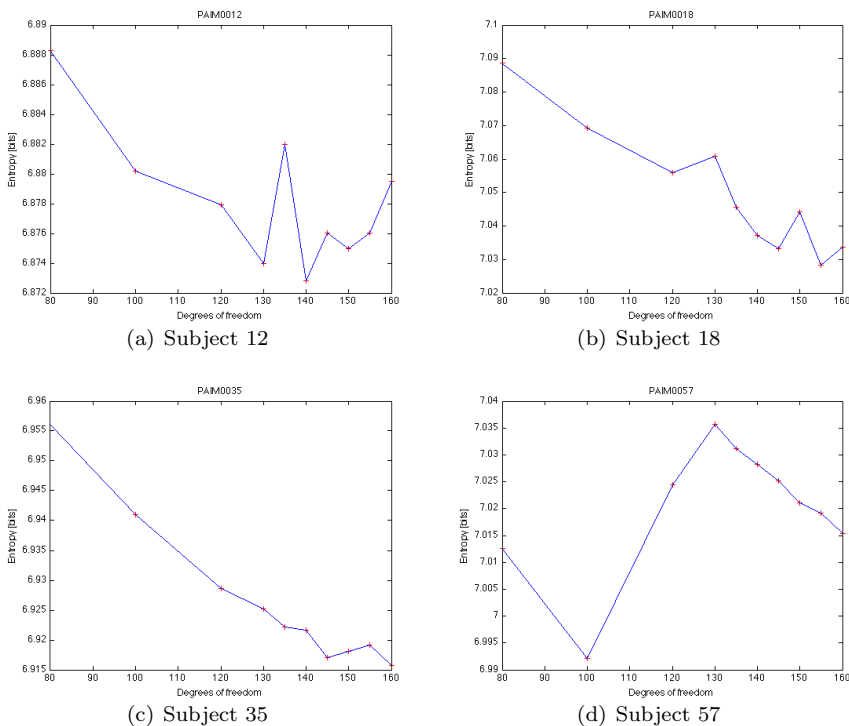


Figure 3.3: Plot of the entropy as a function of the *degrees of freedom* of subject 12, 18, 35, and 57. The bias field correction is performed using the the *Thin Plate Spline*.

The graphs plotted in Figure 3.3, unfortunately, do not have a common minimum, which would have been the optimal outcome. There is a tendency that the curves have a negative gradient at the starting point at 80 df. This might indicate that the choice of 100 df, which was applied earlier on this particular dataset in the old method, is set too low. In (a), the graph of subject 12, the gradient is positive from 140 df, which makes 140 df the most appropriate choice for subject 12. In the graphs shown for subjects 18, 35 and 57 the gradient is still negative at 160 df and there is no common minimum. This might indicate that the minimum is not reached yet. However, this indication should not be taken too much into account, as there is a risk of incorporating noise to the image if the df value is too large. The investigation indicate, at this point, that

a df value above or equal to 140 is the most appropriate. However, at the end, the choice of effective degrees of freedom is an empirical decision and a tradeoff between many parameters. This will be discussed further in Section 3.3.

3.2.2 N3 - Smoothing distance and deconvolution size

The *Shannon entropies* of subjects 12 and 18 are calculated with the N3 method in *Freesurfer*. This is done in the exact same way as with the TPS correction. Two parameters, the smoothing distance, d , and the deconvolution size, FWHM, have been varied to optimize the correction, as described in Section 3.1.2.

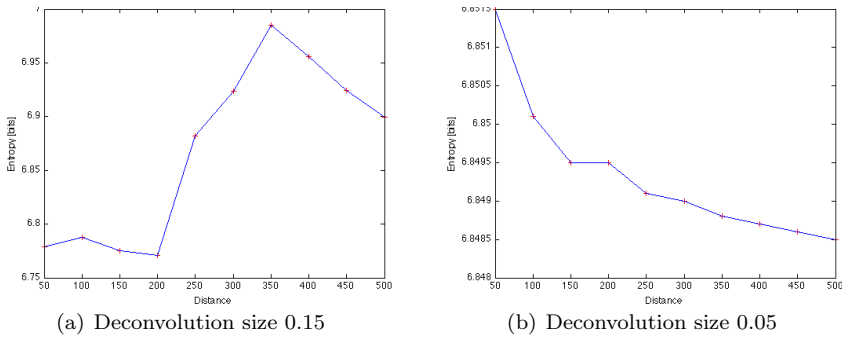
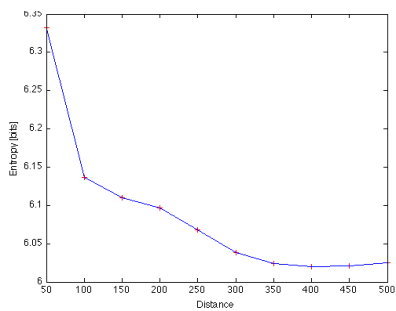
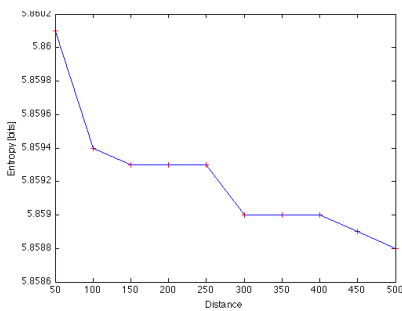


Figure 3.4: Plot of the entropy as a function of the *smoothing distance* of subject 12 with deconvolution size 0.15 (a) and 0.05 (b). The bias field correction is performed using the N3 method.

Figures 3.4 and 3.5 do not give a precise indication of which parameter values that give the best results. From the theory, it is assumed that the smallest value of entropy gives the best correction. The tendency is that the entropy declines as the smoothing distance increases. The tendency is that the entropy is smaller when $\text{FWHM} = 0.05$.



(a) Deconvolution size 0.15



(b) Deconvolution size 0.05

Figure 3.5: Plot of the entropy as a function of the *smoothing distance* of subject 18 with deconvolution size 0.15 (a) and 0.05 (b). The bias field correction is performed using the N3 method.

3.3 Evaluation

The quality of the bias field correction cannot only be based on the entropy, since it has shown ambiguous results. Therefore, it is necessary to look and compare some of the images corrected with the two methods for different parameter choices. Subjects 12 and 35, slice 10 is further looked at. Figures 3.7 and 3.6 show slice 10 of subjects 12 and 35, with two different choices of df to see if it is possible to identify a difference. The first value is 80 df , which according to Figure 3.3 gives a high entropy, while the second value is 145 df which according to Figure 3.3 gives a small entropy. As adipose tissue also include the yellow and light green areas, the intensity difference is reduced and the image has become more homogeneous in Figure 3.6 (b). There is almost no difference in Figure 3.7 where subject 12 is corrected with 80 df and 145 df , respectively. Though, the right image might appear more homogeneous than the left image.

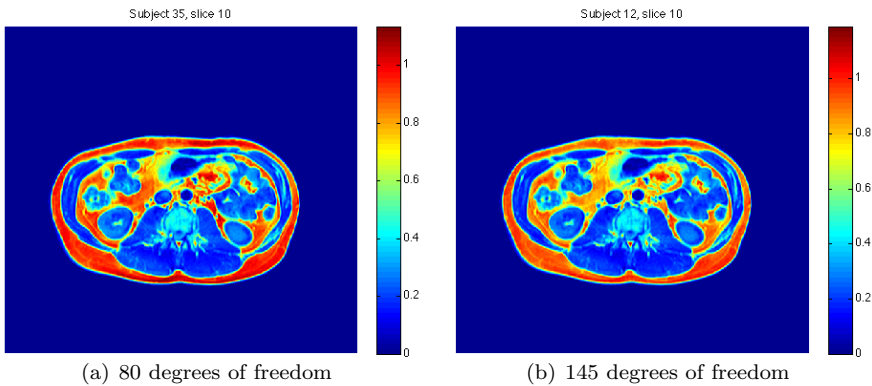


Figure 3.6: Bias field correction of subject 35 slice 10 with 80 degrees of freedom (High entropy) and 145 degrees of freedom (Low entropy).

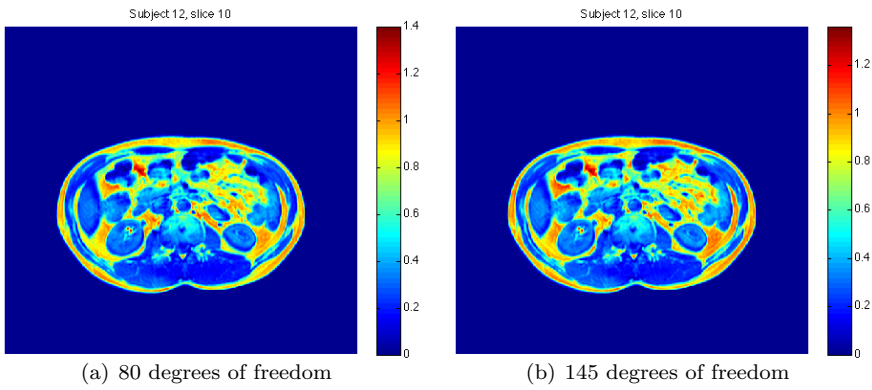


Figure 3.7: Bias field correction of subject 12 slice 10 with 80 degrees of freedom (High entropy) and 145 degrees of freedom (Low entropy).

Figure 3.8 also shows subject 12 slice 10, but here the output is from the N3 method. The FWHM are 0.05 on both slices, but the smoothing distance is 100 mm for the left image and 500 mm for the right image. According to Figure 3.4, a distance equal to 100 mm gives a large entropy, while a distance equal to 500 mm gives a smaller entropy. It is not possible to see a difference between the two slices and still large bias peaks exist in the anterior part of the images. This means, that even voxels belonging to the same-tissue classes have large differences in intensities. By the naked eye it is difficult to see from Figures 3.7, 3.6 and 3.8 that the correction method with a parameter choice giving the smallest entropy is better than the correction method with values giving the highest entropy. This is valid for both the N3 method and the TPS method.

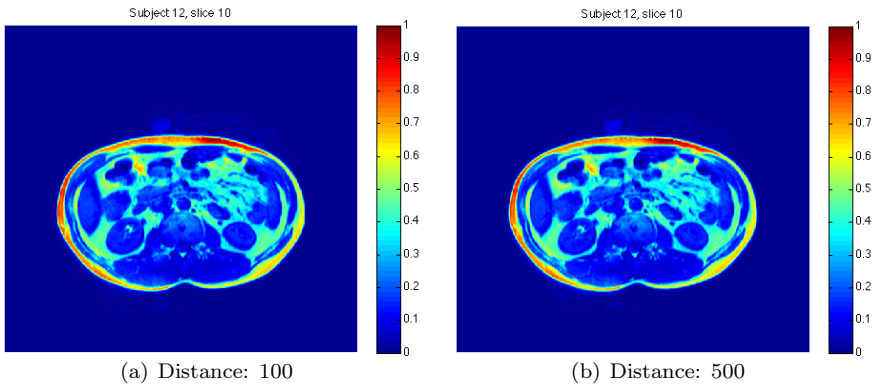


Figure 3.8: Bias field correction of subject 12 slice 10 with $\text{FWHM} = 0.05$ for both images. Image (a) has a smoothing distance of 100 mm (Large entropy) and image (b) has a smoothing distance of 500 mm (Small entropy).

Several subjects are corrected with the N3 method. The corrected images showed a general tendency of not having well defined classes of tissue and are accordingly, not included in this thesis. This method is therefore empirically considered useless for solving this particular problem. The N3 correction in *Freesurfer* is developed for bias field correcting brain MRI data and not abdominal MRI data. From this point of view it makes sense that better results are obtained using *Thin Plate Spline* which is developed for abdominal MRI data. As N3 now has been tried out, the focus returns to the TPS method, which will be applied on this dataset.

The TPS method is developed for estimating the bias field of abdominal MRI data and gives better defined classes of tissues. It is difficult to decide which df is the most appropriate for the entire dataset. As the bias field is unique for each scan the most appropriate value varies from subject to subject. The outcome of this data-driven investigation is that the df value should generally be larger than first expected. The df value chosen in the old method was 100 df, but the corrections with the smallest entropies are all above or equal to 140 degrees of freedom. Though, it should be taken into account that there is a risk of incorporating noise when the df value is too high. Therefore, the data is corrected with TPS at the effective degrees of freedom of 145 on the basis of the entropies calculated and the images examined because this value is considered to give the best general tradeoff and results.

Locating boundaries using Graph Cuts

After the preprocessing described in Chapter 3, the data is ready to be segmented into different types of adipose tissue based on the location in the abdomen. First step is to locate three different boundaries, the abdomen boundary, the interior SAT and Scarpa's Fascia. The boundaries can be seen in Figure 4.1. The abdomen boundary has already been found when preprocessing the data.

Segmentation of the interior SAT and Scarpa's Fascia will be done using a *Graph Cut* approach, which divide the image series into "object" and "background". This is done by constructing a 3D graph, applying Graph Cut theory and finally using an algorithm for cutting made by Yuri Boykov and Vladimir Kolmogorov [6] called *Maximum Flow / Minimum Cut*. This chapter describes the construction of the graph and the above-mentioned algorithm.

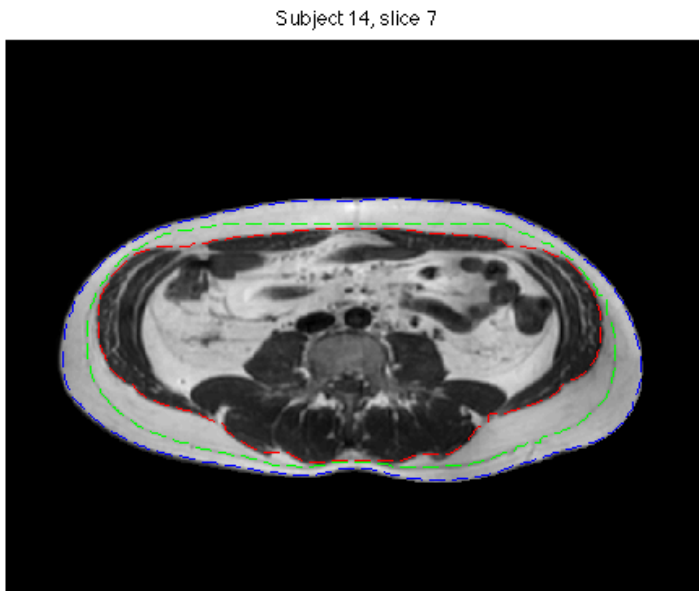


Figure 4.1: Cross section of the abdomen showing three boundaries of the abdominal wall, the abdomen (Blue), Scarpa's Fascia (Green) and the interior SAT (Red) in subject 14 slice 7.

4.1 Graph theory

By definition a weighted graph $G = (V, E)$ is a set of nodes/vertices, V , and a set of edges, E , which connect the nodes. The nodes correspond to voxels in 3D [3]. Each edge has an associated cost/weight/capacity, from now on denoted capacity, which is found from given characteristics in the object of interest, for example local intensity gradients, laplacian zero-crossing or other criteria. Two special nodes exist called *terminals*. One is denoted *Sink-Node* (T) and the other a *Source-Node* (S). They represent object and background labels, respectively. The edges consist of two different types of links, n-links and t-links. N-links, neighboring links, connect neighboring nodes in a regular grid. T-links, terminal links, connect nodes to terminals [3], [6]. The total capacity function is given by:

$$E(f) = E_{n-links}(f) + E_{t-links}(f) \quad (4.1)$$

where $E_{n-links}(f)$ are the capacity of the n-links and $E_{t-links}(f)$ are the capacity of the t-links. A graph is *undirected* when two nodes only have one link, Figure 4.2 (a). The graph is *directed* when two links are present between two nodes. The link in one direction has a capacity whereas the link in the reverse direction can have a different capacity associated, Figure 4.2 (b) [4].



Figure 4.2: (a) Undirected graph: One link from node p to node q. (b) Directed graph: Two links, one from node p to node q and a reverse from node q to node p. The two links can have different capacities [4].

4.2 Graph Cuts

Graph Cuts are used when it is necessary to distinguish "object" from "background". This is done by making a *s-t cut*, C , in a subset of edges $C \in e$, which separates the source and the sink so no dipath can be established from S to T . In the following s-t cuts are referred to as cuts. The capacity of the cut is the total capacity of the edges in the cut:

$$|C| = \sum_{e \in C} E_e \quad (4.2)$$

The best cut is the most efficient way to cut the edges in the graph, so that the object is separated from the background. This is also called a minimum cut, because it has the minimum capacity among all cuts [3]. According to the theorem of *Ford and Fulkerson* the minimum cut can be solved by finding the maximum flow from the *source* to the *sink*. As a visual illustration of the maximum flow, the edges are representing pipes with capacities equal to the edge weights. The *Maximum flow* is the maximum amount of water that can be sent from the sink to the source by the pipes [6].

To be able to separate object from background, it is necessary to use seeds which indicate whether or not a given area belongs to the object or the background [4]. This can be done manually or automatically, and is illustrated in Figure 4.3 (a). In Figure (b), a graph is built based on the the illustration in Figure (a). The capacities of the edges are illustrated by the thickness of the links. Figure (c) shows the minimum cut solved by finding the maximum flow. In Figure (d), the segmentation result is shown, which separates the image into two classes, object and background, respectively [5].

Many *Maximum Flow / Minimum Cut* algorithms exist. Most of the algorithms belong to one of the two following groups: Goldberg-Tarjan style 'push-relabel' methods and algorithms based on Ford-Fulkerson style 'augmenting paths' [6]. The algorithm used in this thesis is developed by Yuri Boykov and Vladimir Kolmogorov. This new *Maximum Flow / Minimum Cut* algorithm is based on *Augmenting path* algorithms, for which reason this kind of algorithm will be shortly described, before the new algorithm is described in details.

The 'augmenting path' algorithms pushes flow from the source to the sink by paths. When these paths are saturated the maximum flow is achieved. The information about the distribution of the current $s \rightarrow t$ flow, f , among the edges of G are stored in a *residual graph* G_f . The capacity of the edge in G_f is dependent on the amount of flow already in the edge. Before any flow is pushed from the source to the sink the edge capacities in G_f are the same as the original graph G . At each new iteration the algorithm finds the shortest path from s to t , were the edges of the residual graph are unsaturated. When a path is found, the algorithm pushes the maximum possible flow df that saturates at least one edge in the path. The residual capacity of edges in the path are reduced by df whereas the residual capacity of the reverse edges increases by df . When any $s \rightarrow t$ path crosses at least one saturated edge in the residual graph the maximum flow is reached and the minimum cut is found [6].

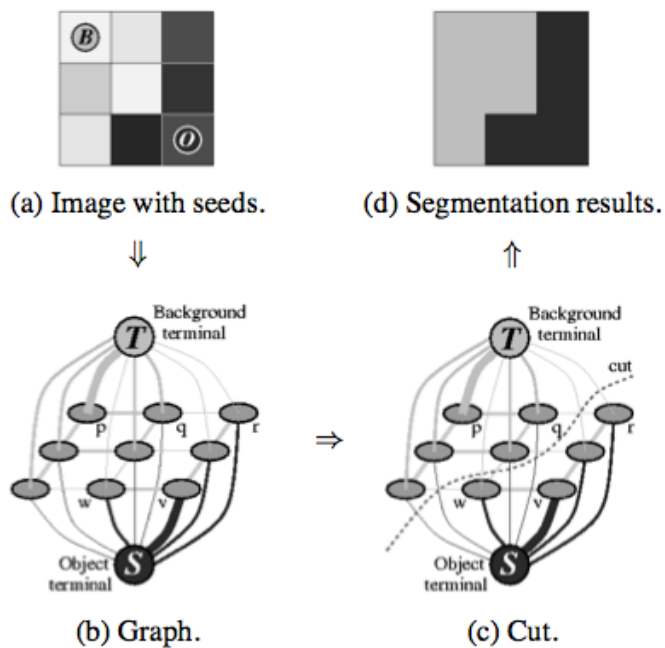


Figure 4.3: Illustration of graph cutting in a 3x3 image. (a) Image with object and background seeds. (b) Graph, with edge capacities illustrated by the thickness of the links. (c) Minimum cut solved by finding the maximum flow. (d) Segmentation result [5].

4.2.1 New Maximum Flow / Minimum Cut algorithm

The new *Maximum Flow/ Minimum Cut* algorithm used in this thesis is based on the *augmenting path* algorithm described above. The algorithm builds search trees for finding the augmenting path. In this algorithm two search trees are built. One from the sink and one from the source. These search trees are reused, which means that new search trees are never built from scratch. This fact influences the run time making the new algorithm 2-5 times faster than earlier developed algorithms [6].

Two non-overlapping search trees S and T exist with roots at the source s and sink t respectively. Tree S has nonsaturated edges from each parent node to its children, whereas in tree T, the edges from children to their parents are non saturated. The nodes which are not a part of tree S or T are called *free*. In both trees active and passive nodes exist. The active nodes are the outer border in each tree, and the passive nodes are internal. Active nodes allow the trees to grow by acquiring new children from free nodes along nonsaturated edges. The passive nodes cannot grow because they are blocked by other nodes from the same tree. As soon as an active node in one tree detects a neighboring node that belongs to the other tree, an augmenting path is found [6]. This is illustrated in Figure 4.4.

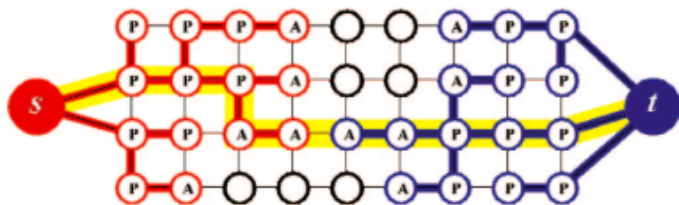


Figure 4.4: Illustration of the search trees S (red nodes) and T (blue nodes) at the end of a growth stage when a path (yellow line) from the source to the sink is found. Active nodes are labeled by the letter A, and passive by the letter P. Free nodes are black [6].

The following three steps are repeated in the algorithm:

1. *Growth stage.* The two search trees S and T grow until they reaches each other, which give a $s \rightarrow t$ path.
2. *Augmentation stage.* The found path is augmented. Search trees break into forests.

3. *Adoption stage.* The trees S and T are restored.

The search trees expand in the *Growth stage*. This is done by the active node which explores neighboring non-saturated edges and gain new *children* nodes from a set of free nodes. These new nodes become members of the search trees. A node becomes passive, when all nodes surrounding the node are explored. The growth stage terminates when an active node explores a neighboring node belonging to the other search tree, and a path is established from the source to the sink. In the *augmentation stage* the path found in the *Growth stage* is augmented. The largest flow is pushed from the sink to the source, which means that some edges become saturated whereas others do not. When some of the nodes have saturated edges that connect them to their parents, they are called *Orphans*. If this is the case, the search trees S and T are split into forests. The source and sink are still roots of the trees S and T, while the orphans form roots for all other trees. In the *adoption stage* the goal is to restore the tree structures of S and T. This is done by trying to find a new valid parent for each orphan. A new parent should belong to the same tree, S or T, as the orphan, and should be connected through a nonsaturated edge. If no valid parent exists for an orphan, the orphan is removed from the tree, S or T, and becomes a free node. The *adoption stage* ends, when no orphans are left, and the tree structures S and T are restored. After the *adoption stage* the algorithm returns to the *growth stage*. The algorithm is terminated when no free nodes exist, which means that the search trees S and T cannot grow and are separated by saturated edges [6].

4.3 Graph Construction

In constructing the graph which corresponds to the 3D dataset, the connection between the nodes, sinks and sources have to be described and assigned with given capacities. The slices of the abdomen can be represented as a 3D volume, $I(x,y,z)$. The goal is to locate two boundaries in the 3D volume, interior SAT and Scarpa's Fascia. According to Li et al. [10] it is possible to locate multiple boundaries at a time using Graph Cuts. However, in this project, the interior SAT boundary will initially be located and then Scarpa's Fascia, because information from the first cut is used as an input to the second. The wanted boundaries are both located in between the abdomen boundary and the center of the image. For this reason, the sink is located on the abdomen boundary, while the source is located at the center of the image. Both sink and source run through the entire volume as a cylinder. A 2D case is shown in Figure 4.5.

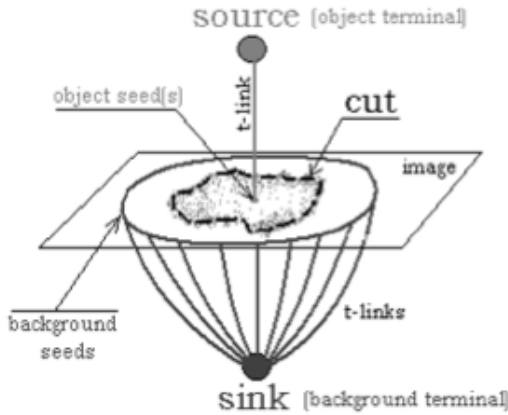


Figure 4.5: Image of one slice with a source at the center and sink on the outer boundary [4].

Instead of using a single voxel as the source, an ellipse placed at the center, is used. This is done to restrict the solution space and remove misleading information by excluding the part of the image in the middle, where the boundary is not located. By using an ellipse, the segmentation will be more robust. When the slice number increases, the area of the abdomen increases, and the mask of the Interior SAT boundary increases as well. By using a MATLAB function called *Imerode* it is possible to increase the size of the source from slice to slice, which means that unnecessary information is excluded. The t-links, linking the sink to the abdomen boundary and the source to the ellipse are given infinity capacities. This ensures, that the flow and the cut will be between the ellipse and the abdomen boundary.

The interior SAT boundary is characterized by a large radial gradient, which can be found slice by slice by the following formula.

$$\frac{dI}{dr} = \left(\begin{array}{c} \frac{dI}{dx} \\ \frac{dI}{dy} \end{array} \right) \cdot \hat{r} \quad (4.3)$$

where \hat{r} is the unit vector from the center of the image to all voxels in the given slice. By applying a gaussian filter with standard deviation equal to 2, the data is smoothed so sharp edges not belonging to the object of interest are blurred, whereas the interior SAT boundary becomes more visible. Figure 4.6 shows the radial gradient in subject 20 slice 1 before and after the gaussian filter is applied. It is clear that the interior SAT boundary is more visible when the filter is used.

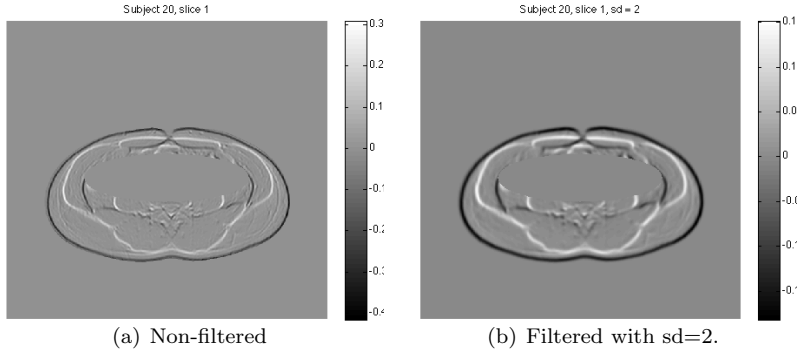


Figure 4.6: Radial gradient of subject 20, slice 1. The center part of the slice is removed using an ellipse. b) Filtered with a standard deviation equal to 2.

Unfortunately, the ellipse in two subjects were placed in a way that the interior SAT boundary was erased. In these two subjects the center of the ellipse was moved a little which lead to a good segmentation result. In the m-file *getInteriorSAT.m* in Appendix E it is denoted in which subjects the ellipse were removed and how much. In one subject the ellipse had to be enlarged to give satisfying results. This is also stated in the m-file.

A node has one link to each neighboring node. This means that a node has two links in each direction, which gives 6 links in 3D. However not all voxels have 6 neighbours. If the slices in a subject are considered a 3D volume, the nodes in the 8 corners have 3 links. The nodes on the edges have 4 links and the nodes on the surface have 5 links, whereas all others have 6 links. From this a vector describing the connections is constructed.

The capacity, β of a link, l , from node, p , is calculated from the filtered radial gradient $\frac{\partial I}{\partial r}$, by the formula:

$$\beta_l = \max\left(\frac{\partial I}{\partial r}\right) - \frac{\partial I(p)}{\partial r} \quad (4.4)$$

This ensures that no negative capacities exist. A large radial gradient corresponds to a low capacity of the link from the node. The depth capacity is a constant that has to be chosen experimentally. If this constant is large compared to the capacities in the horizontal and vertical direction, the algorithm will use too much information from the neighboring slices. In the extreme case

the cut will be the same in all slices. However, if the value is small compared to the other capacities, no or very little information will be used, causing the same result as if applying the algorithm in 2D.

The *Maximum Flow / Minimum Cut* is found using the Boykov and Kolmogorov algorithm [6] described in section 4.2.1, with the inputs: n-capacities, t-capacities and total number of nodes. The code by Boykov and Kolmogorov is made in C++. To be able to run it from *MATLAB*, a C++ wrapper is used [14]. The result is the location of the interior SAT boundary in all slices. The cut is shown for subject 28 slice 2 as a mask and as a boundary superimposed on the original image in Figure 4.7.

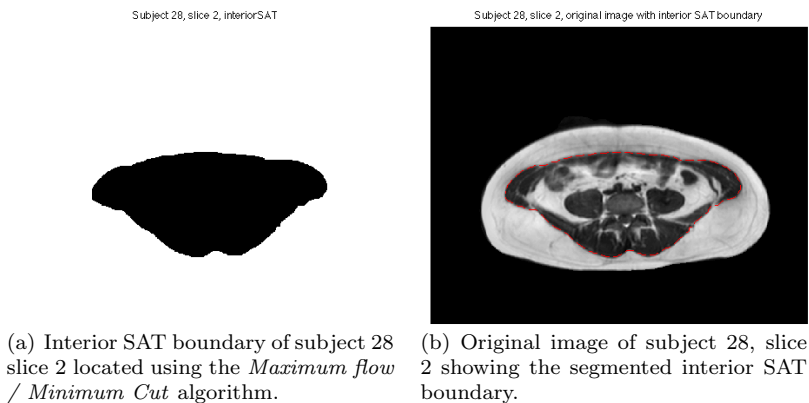


Figure 4.7: Results of the segmentation of the interior SAT boundary in subject 28, slice 2, using *Graph Cuts*.

4.3.1 Scarpa's Fascia

The graph used when locating Scarpa's fascia is constructed in a similar way as the graph of the interior SAT boundary. The difference is that the Scarpa's Fascia is characterized by a large second order derivative. The interior SAT boundary is used as the source, with t-links given a high capacity to ensure a flow through these edges in the *Maximum Flow / Minimum Cut* solution. The sink is defined as the abdomen boundary and is given a high capacity as well. The second order derivative is calculated and the edge capacities are found from the formula:

$$\beta_t = \max\left(\frac{\partial^2 I}{\partial r^2}\right) - \frac{\partial^2 I(p)}{\partial r^2} \quad (4.5)$$

The abdomen boundary, corresponding to the sink, is reduced to restrict the solution space. Likewise, the interior SAT boundary, corresponding to the source, is enlarged. The restricted second order derivative is shown in Figure 4.8.

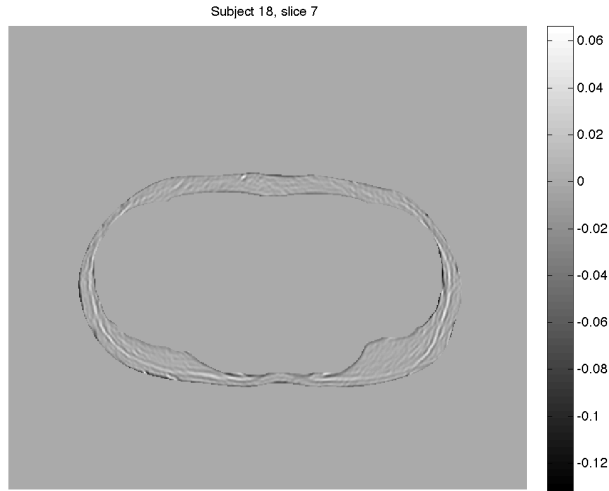


Figure 4.8: Second order derivative of the SAT rim of subject 18, slice 7, where the mask of the interior SAT boundary is used as the source by which the middle part of the image is removed.

Scarpa's Fascia is now found by using the algorithm by Boykov and Kolmogorov, which result in a segmentation of Scarpa's Fascia in all slices. The bias field corrected image of subject 18, slice 7, is shown in Figure 4.9 together with the segmented Scarpa's Fascia superimposed on the bias field corrected image.

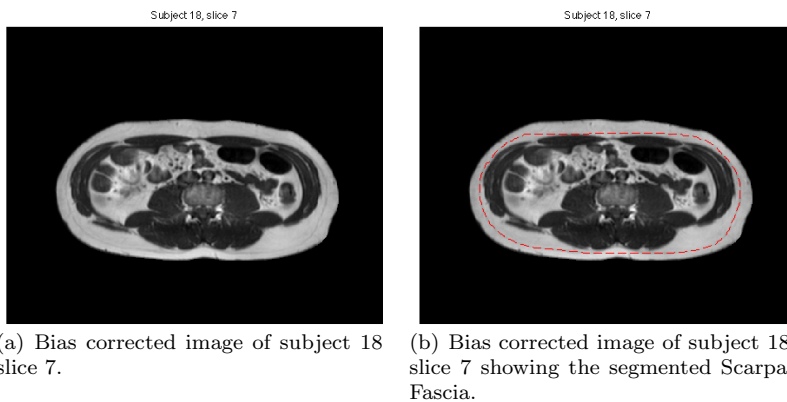


Figure 4.9: Results of segmentation of Scarpas Fascia in subject 18, slice 7, using *Graph Cuts*.

4.4 Evaluation

Applying the *Maximum Flow / Minimum Cut* algorithm to locate the interior SAT boundary and Scarpa's Fascia, overall seems to be a suitable choice. However, the algorithm does not locate the boundaries correctly through the entire dataset. This is especially a problem when locating Scarpa's Fascia. If Figure 4.8 is considered, it is clear, that Scarpa's Fascia is very hard to identify. Scarpa's Fascia is almost impossible to see visually in the anterior part of the abdomen in almost every slice. However, the algorithm chooses the shortest way when it loses track of the second order derivative, which means, that a subdivision is present in the anterior part of the abdomen. The old method tracked the interior SAT boundary, when the Scarpa's Fascia was not visible, which resulted in no subdivision of the SAT layer in the anterior part of the abdomen. The old method was better detecting the details of the Scarpa's Fascia in the posterior part of the abdomen.

The *Graph Cut* method has generally some problems locating the boundaries when they approximate the radial gradient. In Figure 4.10 the radial gradient of a subject 8, slice 3, is shown. The blue arrow points out an area where the radial gradient is blurred because it follows the interior SAT boundary. In the left side, the SAT boundary is not continuous in the original image and therefore the radial gradient is not visible in the figure.

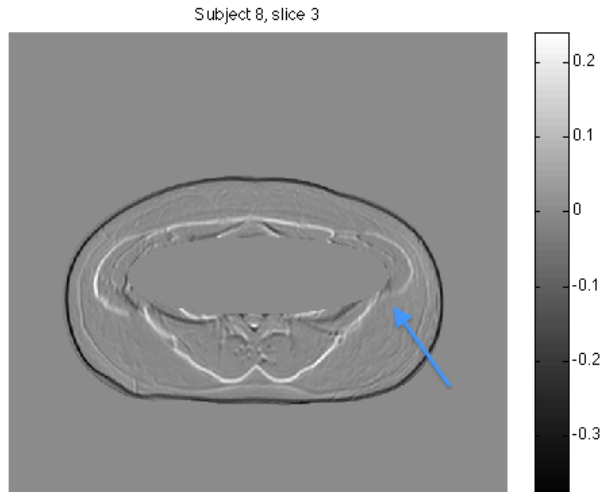


Figure 4.10: Subject 8 slice 3, showing the radial gradient.

It is possible to adjust the capacities to change the smoothness term. The ratio of the horizontal and vertical capacities determines the smoothness. Enlarging the capacities in one direction makes the cut more detailed in that specific direction. This leads to a less detailed cut in the other direction. According to this, the capacities are calculated the same way in both directions. If the radial gradient of the interior SAT boundary is not continuous or visible, it is possible to apply a wider gaussian filter. This makes the interior SAT boundary more visible and easier to segment. A wider gaussian filter, $sd = 4$, is applied on 4 subjects, which make the segmentation more inaccurate.

The results were shown to Martin Bæk Petersen, a pregraduate research student in medicine at the *FINE* project. Overall he seemed happy with the segmentation results concerning the interior SAT boundary. Because the smoothness of the segmentation, fine details of the interior SAT boundary are missing. Especially, one place in the posterior part of the slices an error occurs, Figure 4.11. This error seems to be systematic.

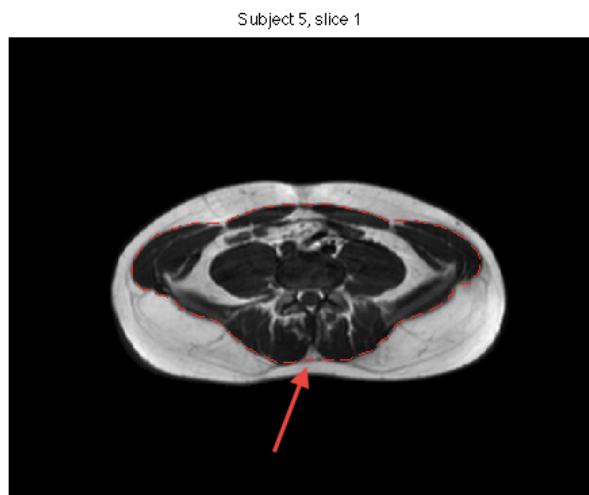


Figure 4.11: Subject 5 slice 1, showing the bias corrected image together with the segmented interior SAT boundary. The arrow points at a detail, where the algorithm fails to segment the boundary accurately in almost every slice.

Martin Bæk Petersen confirmed, that the segmentation of Scarpa's Fascia was better than the old method, but estimated that the method was not yet good enough to be used in clinical research. As it does not track Scarpa's Fascia in all slices and when it does, the fine details are missing. However, he was

impressed that it could locate Scarpa's Fascia well in slices with a small SAT rim. By looking at the input to locate Scarpa's Fascia it seems clear, why the algorithm has difficulties locating the boundary. Scarpa's Fascia is not visible trough the entire SAT layer. It is unknown whether this has something to do with the quality of the scans, the bias field correction, or simply the fact that the boundary is not visible.

Figure 4.12 shows a 3D plot of the SAT rim of subject 2 divided into dSAT (brown) and sSAT (green). The figure is based on the 3 boundaries segmented. The plot is made to visualize that the program operates in 3 dimensions.

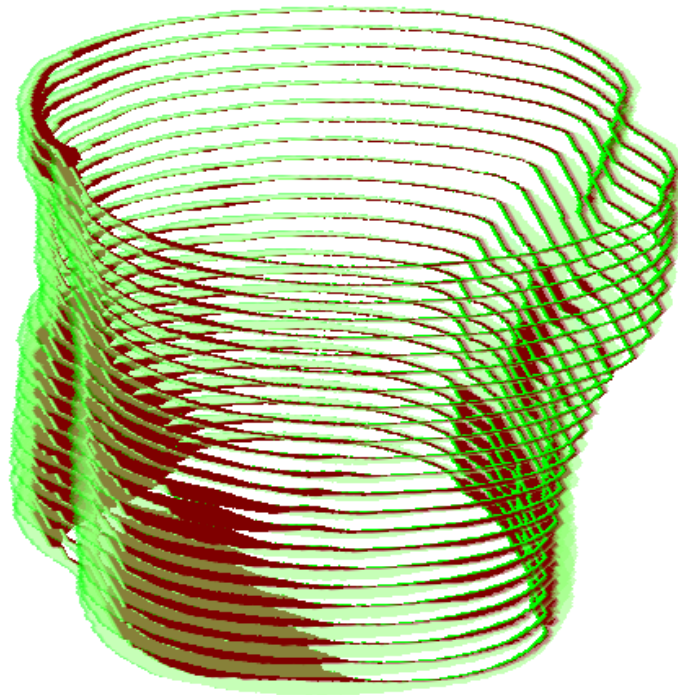


Figure 4.12: 3D plot of subject 2. Brown; dSAT. Green; sSAT.

Segmenting regions

After the boundaries have been found using the *Maximum Flow / Minimum Cut* algorithm, the abdomen has to be divided into VAT, dSAT and sSAT. To be able to do that, it is necessary to distinguish adipose tissue voxels from non-adipose tissue voxels. This will be done comparing two different approaches: *Fuzzy C-means Clustering* and *Graph Cut*. When the division of the abdomen into the classes has been done, the classification of the different types of adipose tissue will be proceeded.

5.1 Identifying Adipose Tissue

After the Bias field correction described in Chapter 3, the intensity histogram generally shows two peaks. One peak at low intensities corresponding to non-adipose tissue voxels and a peak at high intensities corresponding to adipose tissue voxels. This indicates a possibility of identifying the adipose tissue from the non-adipose tissue using an intensity-based approach separating the histogram peaks. This can be done using a technique called *Fussy C-means Clustering* (FCM), described in this section. The FCM method is used in the old method. Another approach is to separate 'Object' (adipose tissue) from 'Background' (non-adipose tissue) using *Graph Cuts*. The general *Graph Cut* theory and al-

gorithm have been described in Chapter 4, and will not be described in this chapter, but the Graph construction in this case will be considered.

5.1.1 Fuzzy C-means Clustering

In this particular dataset two types of clusters are present, non-adipose and adipose clusters. In abdominal MRI no distinct split into the classes considered, exists. The category membership of a given voxel is fuzzy, which means that a voxel to a certain degree belongs to both clusters. The FCM assigns the voxel a fuzzy category membership with an estimated probability that the voxel belongs to the cluster [8]. FCM seeks a minimum of a criterion function, J_{FCM} , which expresses the quality of the clusters identified by a weighted sum of squared distances:

$$J_{FCM} = \sum_{j=\Omega} \sum_{k=1}^C u_{jk}^q |y_j - v_k|^2 \quad (5.1)$$

Where j denotes a voxel location in the image domain Ω , k is the class index, C is the number of classes. The parameter u_{jk} lies between 0 and 1 and express the fuzzy membership value of class k for voxel j . q is a weighted exponent higher than 1 defining the fuzziness of the classifications. y_j is the intensity of voxel j and v_k is the centroid of the class.

The criterion function J_{FCM} is minimized with respect to u_{jk} and v_k by iterative updating of two equations defining u_{jk} and v_k .

There are two classes, $C=2$. Because $q = 2$ a smooth membership curve exists but also a high degree of fuzziness.

After calculating the fuzzy membership value of each voxel a labeling function $f(j)$ is defined as:

$$f(j) = \begin{cases} 1 & \text{if } u_{jk} \geq \varepsilon_m \\ 0 & \text{if } u_{jk} < \varepsilon_m \end{cases} \quad (5.2)$$

where $f(j) = 1$ is a label of adipose tissue. $\varepsilon_m = 0.85$, as this value gives the best tradeoff when defining which membership values actually belong to the adipose tissue region.

Figure 5.1 shows slice 4 of subject 18, where the FCM has been applied to cluster the image into adipose and non-adipose tissue.

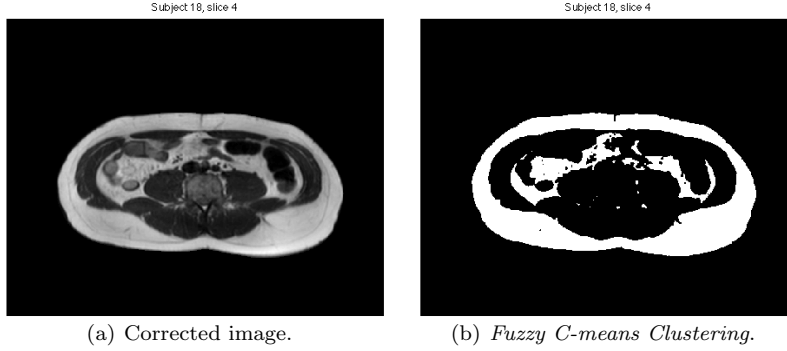


Figure 5.1: Subject 18, slice 4. Showing the bias corrected image and the clustered image using *Fuzzy C-means Clustering*.

5.1.2 Graph Cut

To be able to use *Graph Cuts* to distinguish between adipose tissue and non-adipose tissue, a graph has to be constructed. The graph is built in 2D. The number of nodes are equal to the number of voxels in a slice. Each node has 4 neighbors in the plan. A node has two t-links, one that connects it to the source (s), representing adipose tissue, and one to the sink (t), representing non-adipose tissue. This is illustrated in Figure 5.2.

The t-links are given capacities by the following formula derived from the Mahalanobis distance [1]:

$$U_{nonfat} = \frac{\log(\det(\sigma_{nonfat}^2)) + (y_{ij} - \mu_{nonfat})^T \cdot \sigma_{nonfat}^2{}^{-1} \cdot (y_{ij} - \mu_{nonfat})}{2} \quad (5.3)$$

$$U_{fat} = \frac{\log(\det(\sigma_{fat}^2)) + (y_{ij} - \mu_{fat})^T \cdot \sigma_{fat}^2{}^{-1} \cdot (y_{ij} - \mu_{fat})}{2} \quad (5.4)$$

where y_{ij} is the normalized intensity at a given voxel $v(i, j)$, σ^2 is the variance and μ is the mean of the adipose tissue or non-adipose tissue, respectively.

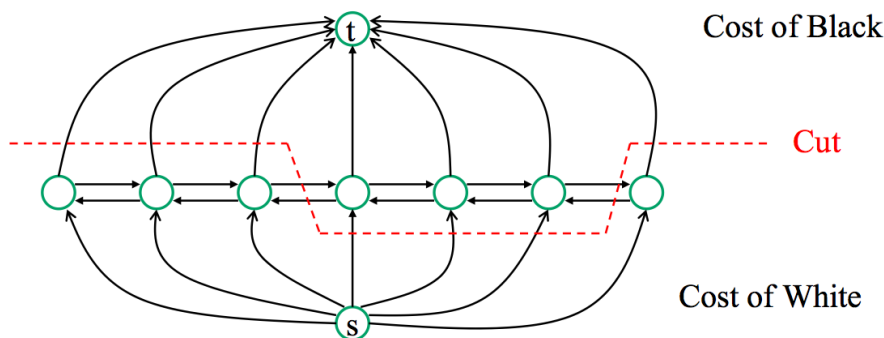


Figure 5.2: Illustration of Graph construction and cutting of one slice. The nodes in the horizontal line represent voxels in a slice. The sink (t) represents non-adipose tissue (black) and the source (s) represents adipose tissue (White). The red dotted line represents the minimum cut [11].

The variance and mean can be found using a function in *MATLAB* called *Roipoly*. The user specifies a polygonal by pointing out the vertices of the polygonal. From this polygonal, the mean and variance are calculated. In this case a non-adipose tissue region and an adipose tissue region are selected which is shown in Figure 5.3.

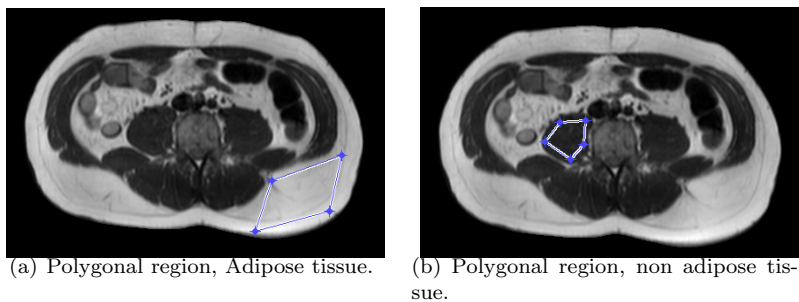


Figure 5.3: Polygonal region specified by the user from which the mean intensity and standard deviation are calculated.

The means and standard deviations from the adipose and non-adipose tissue regions together with the image intensities are used as input in Equation 5.3 and Equation 5.4. Equation 5.3 gives the t -capacities for the sink (t), non-adipose

tissue, while Equation 5.4 gives the t-capacities for the source (s), adipose tissue. All n-links are given zero capacity. The t-capacities, n-capacities and the total number of nodes are given as input to the *Maximum Flow/ Minimum Cut* algorithm. This gives a cut, which separates adipose tissue from non-adipose tissue. The cut is illustrated graphically in Figure 5.2.

Figure 5.4 shows subject 18, slice 4. (a) is the bias corrected slice. (b)-(d) show the division of adipose and non-adipose tissue using *Graph Cuts* where the means and standard deviations are calculated from different regions of varying size. The figures are quite similar, but the best result is achieved in Figure (d), where large regions are chosen. The homogeneity of the region is a factor to be considered. If the region is very large, its probability of being homogeneous is small, which results in a calculated mean and variance of the particular tissue, not representative for the image. The best result is obtained when the area is as large and homogeneous as possible.

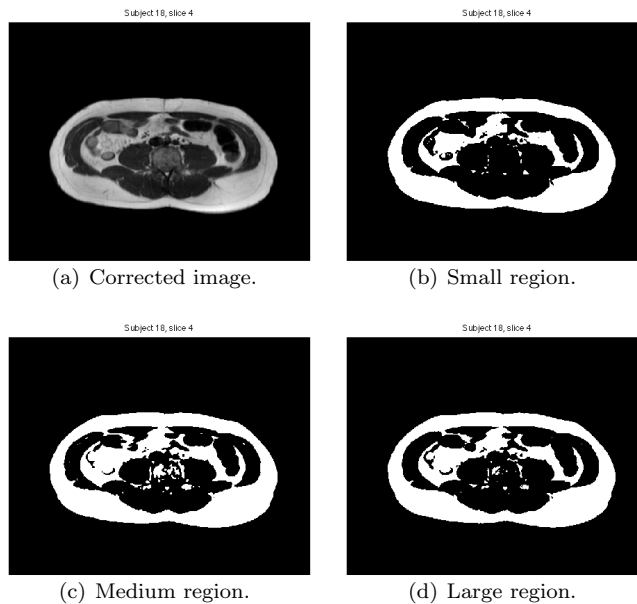


Figure 5.4: Subject 18, slice 4. (a) Showing the corrected image. (b)-(d) Showing the division of the abdomen into adipose and non-adipose tissue using the *Graph Cut* method with different sizes of regions chosen when calculating the mean and variance.

5.2 Evaluation

Using FCM and *Graph Cut* to cluster the abdomen into adipose and non-adipose tissue generates different outputs that can be compared. Comparing Figure 5.1 and 5.4 indicates, that the *Graph Cut* method determines the volume of adipose tissue larger and more correct than the *FCM* method, especially the VAT volume. However, before clustering with *Graph Cut* the mean and variance have to be calculated in each slice. To be able to develop an automatic segmentation method, the mean and variance found in one slice, should be applied in all slices. In Figure 5.5 subject 24, slice 19, is shown together with two clustered images of the same slice. (b) is clustered using *Graph Cuts*, and (c) using FCM. When clustering using *Graph Cuts* the mean and variance calculated in subject 18, slice 4, are used. If the images in Figure 5.5 are compared, it can be seen, that the FCM method is a bit more accurate than the *Graph Cut* method. The *Graph Cut* method overestimates the amount of adipose tissue. This can be seen in Figure 5.6 where the clustered images using *Graph Cut* and *FCM*, respectively, are shown superimposed on the original slice. If figure (a) is considered some areas are darker green than others. The dark green areas illustrate the places, where the clustering has overestimated the VAT. The overestimation can be eliminated if the mean and variance were calculated for this particular slice. However, this has to be done manually, and because the method has to be automatic, this is not a suitable choice. If it was possible to choose an adipose and a non-adipose region, representing the classes through the entire volume, in all subjects, the mean and variance could be found simultaneously in all slices. As the shape of the abdomen, and the location of the classes, varies a great deal through the volume, this method cannot be used.

Taking the evaluation into account, it is chosen to use the FCM method to distinguish between adipose and non-adipose tissue. However, the *Graph Cut* method would probably give better results, if the mean and variance could be calculated automatically in all slices.

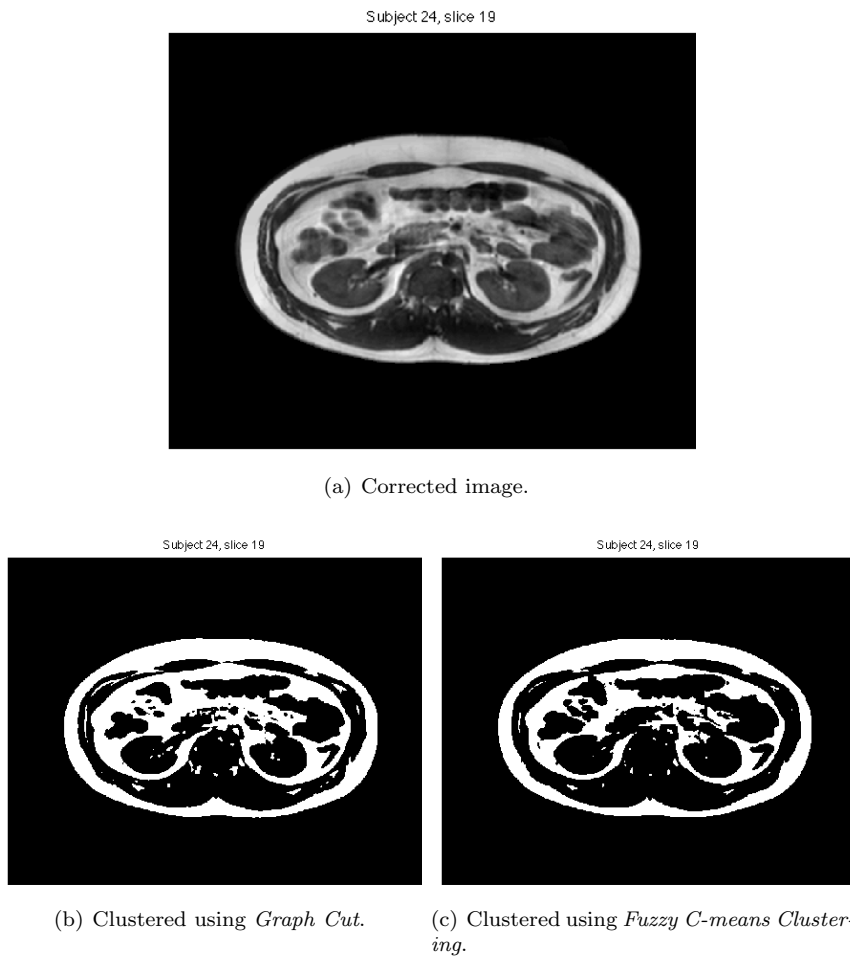


Figure 5.5: Subject 24, slice 19. (a) Corrected image. (b) Clustered image using *Graph Cut*. Mean and variance are calculated from a large polygon area in another subject, Subject 18, slice 4. (c) Clustered image using *Fuzzy C-means Clustering*.

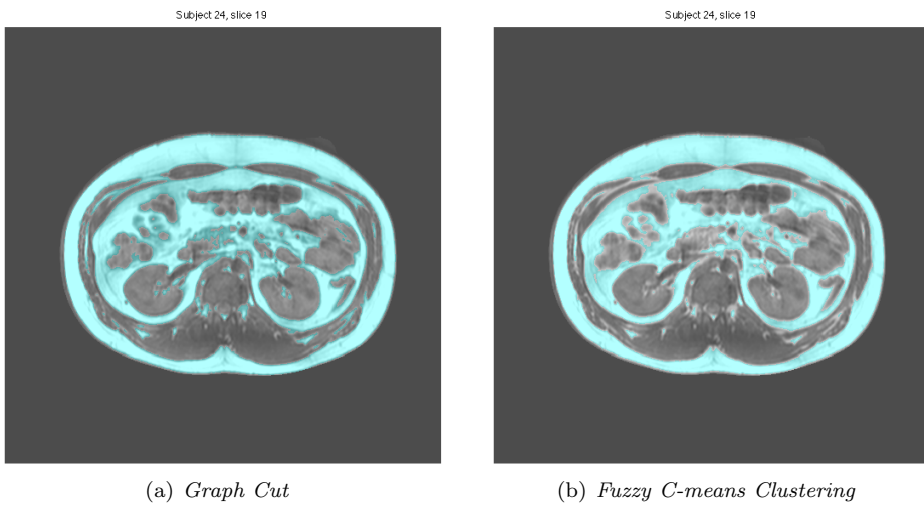


Figure 5.6: Subject 24, slice 19. Original slice with the clustered image superimposed (light green) with (a) *Graph Cut* method and (b) FCM method.

5.3 Segmenting regions

When the abdomen boundary, interior SAT and Scarpa's Fascia are located, and the dataset is clustered, the classification of the abdomen into VAT, dSAT and sSAT, can be done. A binary mask of each of the located boundaries exists. The mask is the same size as the original image, and has the value 1 in voxels inside the mask, and the value 0 in voxels outside the mask. The 3 masks are combined with the clustered images which gives the classification into the 3 wanted adipose tissue classes. Figure 5.7 illustrates the 3 boundaries found in Subject 21, slice 3. Figure (a) shows the slice with the 3 segmented boundaries superimposed. Figure (b)-(d) illustrate the binary masks used when calculating the different classes of adipose.

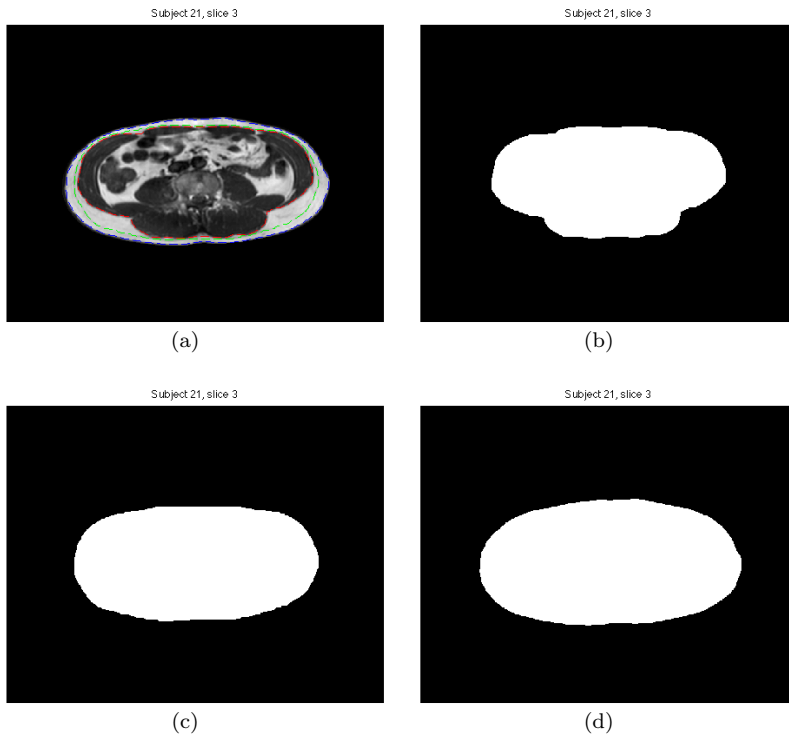


Figure 5.7: Subject 21, slice 4. (a) The corrected image with the three located boundaries superimposed. (b) The interior SAT mask. (c) The Scarpa's Fascia mask. (d) The outer abdomen mask.

The result of the segmentation into the 3 different adipose tissue classes are shown in Figure 5.8 for subject 21, slice 3. White indicates VAT, light grey indicates dSAT, dark grey indicates sSAT and black indicates non-adipose tissue and background. Figure 5.9 illustrates the original slice of Subject 21, slice 3, with a superimposed image of the segmented classes. The classes are 30% transparent, which makes it possible to see the performance of the segmentation. According to the figure, the abdomen boundary is not located accurate everywhere. The same is valid for VAT. Though, the fact of raising the degrees of freedom from 100 to 145, discussed in Chapter 3, seemed to have increased the total fat segmentation. As the old method seemed to be underestimating the amount of fat, this different parameter choice has made the segmentation more accurate. The new and old method will be compared in the next chapter.

Subject 21, slice 3

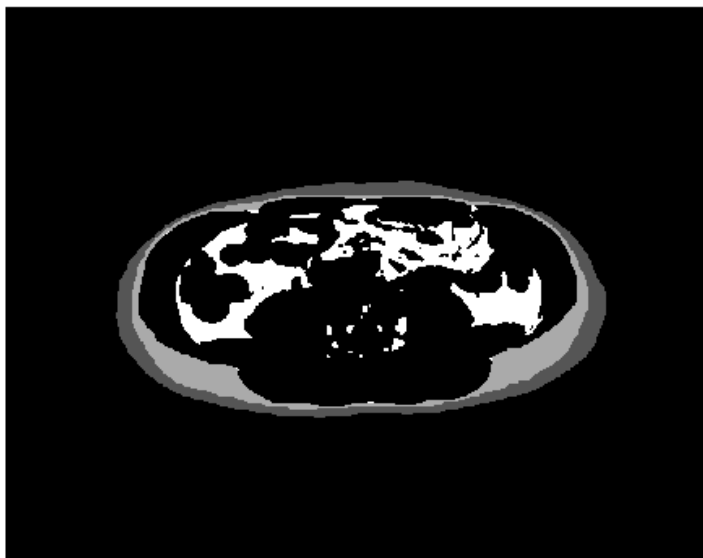


Figure 5.8: Subject 21, slice 3. Division of the slice into VAT (white), dSAT (light grey) and sSAT(dark grey).

Subject 21, slice 3

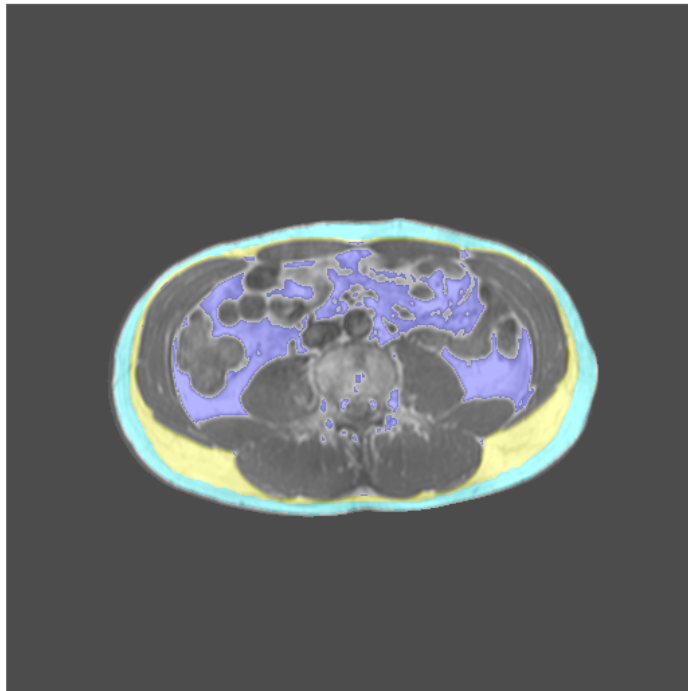


Figure 5.9: Subject 21, slice 3. Showing the original corrected image with the segmentation of the classes superimposed. The classes are 30% transparent.

Final results

This chapter presents the final abdominal segmentation results into VAT, sSAT and dSAT. Furthermore, a statistical analysis is done comparing weight losses with training intensity. A statistical comparison between the final results of the new and old method is executed.

6.1 Segmentation results

The results of the abdominal adipose tissue segmentation is presented in this section. The quantities of the adipose tissue classes are calculated as a percentage of the total voxel volume. The percentages of total fat, VAT, SAT, dSAT and sSAT are included on a CD in Appendix D for all subjects together with the percentages of total fat, VAT and SAT found using the old method. These results are used in the statistical analysis in Chapter 6.2. A closer look at 12 subjects is taken. The 12 subjects correspond to 6 persons, each having a pre and a post scanning. There are two persons from each training intensity group. In Appendix A the quantity of total fat, VAT, sSAT, dSAT and SAT are shown as a percentage of the total voxel volume for these 6 persons together with the percentage loss of total voxel volume in each class of adipose tissue. The voxel volume can be calculated to liters, but this is considered to be unnecessary in the specific case as it has risks of losing information associated.

In Appendix B the segmentation results together with the original images are shown for the 12 chosen subjects. The first slice, middle slice and bottom slice are displayed for the persons together with the corresponding original slice, which makes it possible to visually compare the segmented result with the original image. The rest of the slices are included on the CD in Appendix D together with the entire segmented dataset of all subjects.

6.2 Statistical analysis

On the basis of the data from the intervention study where the subjects are scanned prior to and after 12 weeks of intervention, a statistical analysis is performed. The segmentation was performed blindfolded and it is now revealed which scans origin from the same person. It is relevant to do statistics on the weight losses of the adipose tissue classes according to training intensity groups. Two training intensity groups are prescribed to burn 600 kcal/day, and 300 kcal/day, respectively. The control group should be sedentary. The three groups are called high, h, medium, m, and control, c. In Appendix F the statistical analysis performed in R is enclosed.

A test of the homogeneity hypothesis:

$$H_0 = \mu_1 = \mu_2 = \mu_3 \quad (6.1)$$

$$H_1 = \mu_i \text{ are not all equal, } i = 1, 2, \dots, n \quad (6.2)$$

is performed. The null hypothesis is tested with a one-way ANOVA test for the five adipose tissue groups total fat(VAT+SAT), VAT, SAT, sSAT and dSAT, respectively. As a one-way ANOVA test assumes variance homogeneity, Bartlett's test is performed on the three training intensity groups for each adipose tissue class. The results of Bartlett's test are shown in Table 6.1. The low P-values reveal variance inhomogeneity between the training groups with respect to dSAT and sSAT. On this basis one-way ANOVA tests for total fat, VAT and SAT are performed.

Adipose tissue type	P-value
Total fat	0.07566
SAT	0.0957
VAT	0.131
dSAT	2.134e-13
sSAT	0.01396

Table 6.1: Bartlett's tests of homogeneity of variances.

6.2.1 One-way ANOVA tests

Table 6.2 shows the results of the ANOVA tests. The significance levels are also included in the table.

Adipose tissue type	P-value	F-value	Significance level
Total fat	0.003503	7.1497	1%
SAT	0.006038	6.3122	1%
VAT	0.01503	4.9882	5%

Table 6.2: Results of ANOVA tests

Based on the low P-values the null hypothesis of equal weight losses in the three training intensity groups can be rejected.

6.2.2 Unpaired two sample t-tests

In the following section paired t-tests between two training intensity groups at a time will be performed for the hypotheses:

$$H_0 = \mu_1 - \mu_2 = 0 \quad (6.3)$$

$$H_1 = \mu_1 - \mu_2 \neq 0 \quad (6.4)$$

In Table 6.3, 6.4 and 6.5 the t-values and P-values of the unpaired two sample t-tests between the groups are shown. The significance level is 1%. Three tests are performed for each class: total fat, SAT and VAT. The tests are carried out between the high intensity group and medium intensity group, high intensity group and control group and medium intensity group and control group.

Training intensities compared	t-value	P-value
high & medium	0.7135	0.4847
high & control	4.1641	0.0007315
medium & control	3.0249	0.00805

Table 6.3: Results of two sample t-tests for total fat losses

Table 6.3 shows significant difference between the total fat loss of the high and medium intensity group vs. the control group, respectively. No difference is observed between the high and medium intensity group.

Training intensities compared	t-value	P-value
high & medium	-0.1195	0.9062
high & control	4.1163	0.0008085
medium & control	2.9558	0.009298

Table 6.4: Results of two sample t-tests for SAT losses

Table 6.4 shows significant difference between the SAT loss of the high and medium intensity group vs. the control group, respectively. No difference is observed between the high and medium intensity group.

Training intensities compared	t-value	P-value
high & medium	1.3839	0.1833
high & control	3.4831	0.003071
medium & control	1.8074	0.08954

Table 6.5: Results of two sample t-tests for VAT losses

Table 6.5 shows significant difference between VAT losses of the high intensity group and the control group. No difference is observed between the other groups.

6.2.3 Comparison between segmentation results of the new and old method independent of training intensity groups

To evaluate the segmentation results of the new method, a comparison to the segmentation results of the old method is performed. The segmentation of the SAT-layer into dSAT and sSAT with the old method does not give plausible results, which means that the statistical analysis can only be performed with respect to the following classes: total fat, SAT and VAT.

6.2.3.1 Paired t-tests

The results of the paired t-tests between the amount of total fat, SAT and VAT segmented with the new and old method are shown in Figure 6.6.

Based on the low P-values the null hypothesis, equal means, can be rejected. The results with the new method are significant larger than the old method.

Adipose tissue type	P-value
Total fat	2.2e-16
SAT	2.271e-06
VAT	2.2e-16

Table 6.6: Results of paired t-tests between the new and old method

6.2.3.2 Histograms

To illustrate the deviation between the segmentation results with the old and new method the differences between the results are calculated. The difference is plotted in a histogram containing 25 intervals on the x-axis. The y-axis shows the frequency and the x-axis the percentage difference. A positive value on the x-axis corresponds to a larger estimated volume with the new method. Histograms are made for: total fat (Figure 6.1), SAT (Figure 6.2) and VAT (Figure 6.3).

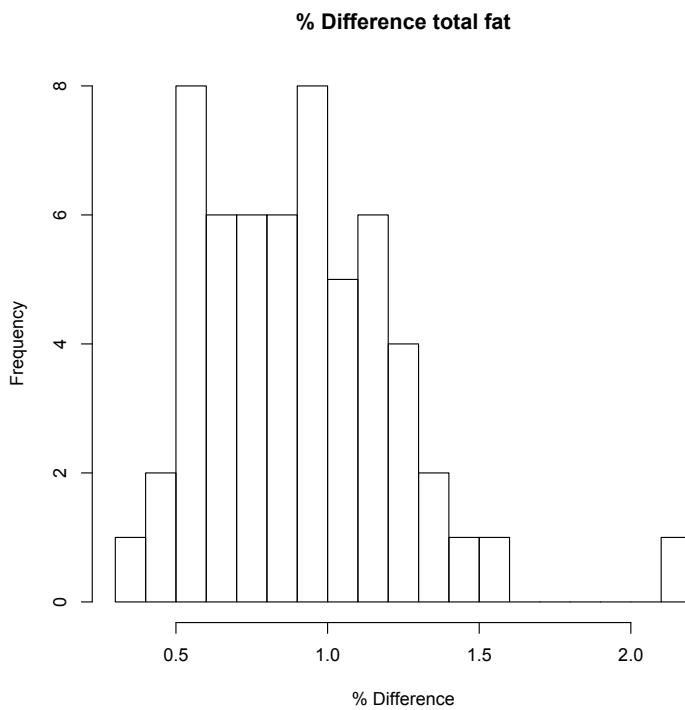


Figure 6.1: Histogram showing the frequency at the y-axis and the percentage difference between the total fat volume of the new and old method at the x-axis.

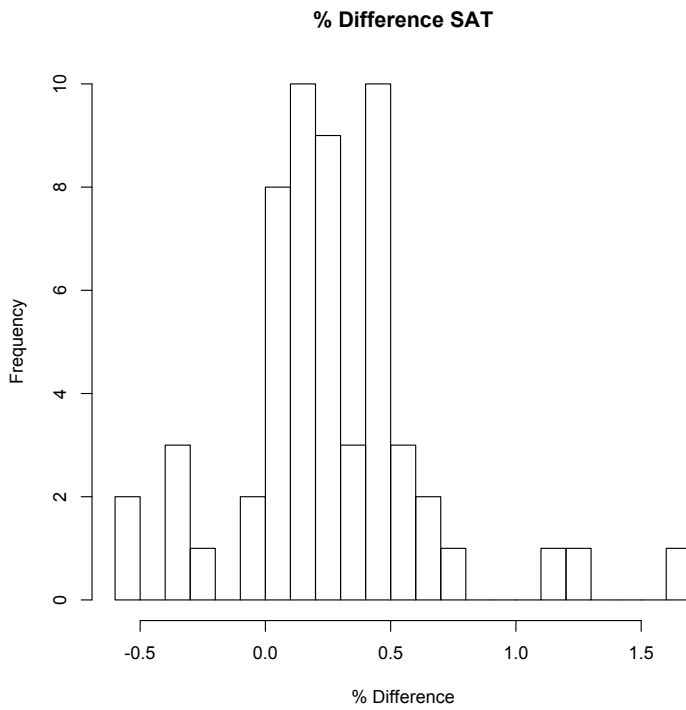


Figure 6.2: Histogram showing the frequency at the y-axis and the percentage difference between the SAT volume of the new and old method at the x-axis.

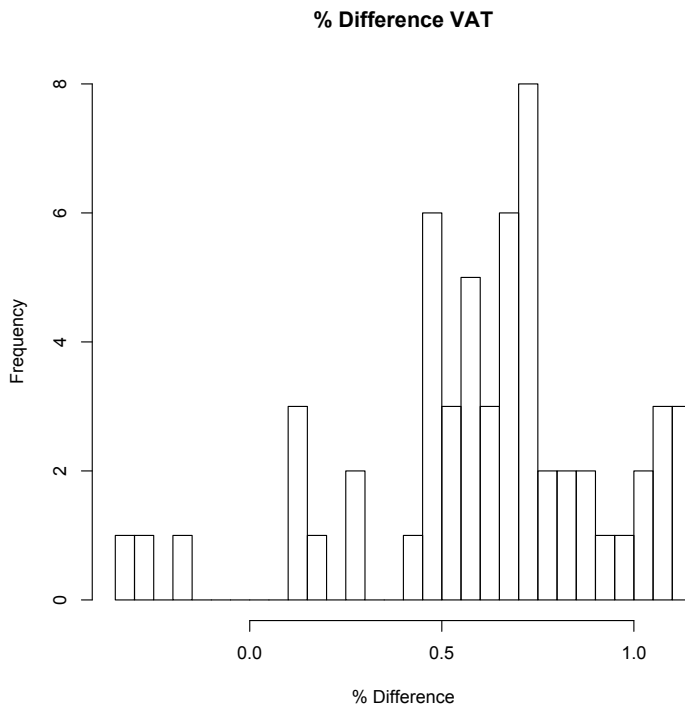


Figure 6.3: Histogram showing the frequency at the y-axis and the percentage difference between the VAT volume of the new and old method at the x-axis.

6.3 Evaluation

As Bartlett’s test for dSAT and sSAT showed, the variances within the three training groups are not equal. This is an indication that Scarpa’s Fascia, which divides the SAT layer into dSAT and sSAT, is not well located in all subjects. This is a weakness of the program. When looking at the segmentation results in Figure B.5 (a), B.7 (a) and B.9 (a) shown in Appendix B it is observed, that location of Scarpa’s Fascia is a bit rough. Especially in the first slices, corresponding to the slices with the largest amount of fat, the fascia is not smooth. Though, when looking at the middle and last slices of all subjects shown in Appendix B the location is quite accurate and smooth, even in the last slices where the fascia is almost impossible to see with the naked eye. In Figure B.8 and B.4, also shown in Appendix B, the location of Scarpa’s Fascia appears precise in all six slices shown. The variance inhomogeneity of dSAT and sSAT could also be due to the fact that there are large variations in Scarpa’s Fascia’s location within the subjects.

A validation of the scan and segmentation quality has been performed to test whether the segmentation is reproducible. Table 6.7 shows two post scans from the same person performed immediately after each other.

	% FAT	% VAT	% SAT	% dSAT	% sSAT
Subject 62 - Post 1	46.73%	20.48%	26.25%	12.14%	14.11%
Subject 67 - Post 2	46.76%	20.51%	26.25%	11.68%	14.57%

Table 6.7: Two post scans from the same person performed immediately after each other. The person is from the control group.

Table 6.7 shows how the estimates of total fat, VAT and SAT is reproducible because of the very small difference in the fat percentages. The SAT is estimated exactly the same for both scans. The estimates of dSAT and sSAT differ from each other with 0.46%, resulting in 0.46% more dSAT and 0.46% less sSAT in one scan and vice versa in the other scan. This gives an indication that the abdomen boundary and the interior SAT boundary are accurately segmented while Scarpa’s Fascia is not located with the same precision.

The one-way ANOVA tests show that there are not equal means in the weight losses of the three intensity groups for total fat, SAT and VAT. The results of the ANOVA test form the basis of performing the unpaired two sample t-test between the training intensity groups. When looking at the results of the

t-tests for high/control and medium/control for total fat and SAT losses the P-values are significant, which means that there has been an abdominal fat loss. This reveals that the training does have an effect on the abdominal fat loss, as the control group is assumed to do no exercises at all. For all three adipose tissue classes, t-tests between the high and medium intensity group, show no significant difference in fat losses. This indicates that the results do not tell whether there is a difference in exercising 1 hour or 1/2 hour a day. As there are no restrictions on the calorie intake during the training period, the subjects belonging to the high intensity group might eat more because the training leads to more appetite. As for VAT there is a significant abdominal fat loss between high and control group which means the subjects in the high training intensity group seem to have lost some of the clinical dangerous adipose tissue. The VAT segmentation, though, is not always reliable because of the clustering method, discussed in Chapter 5. When looking in Appendix B at Figure B.7 and B.8 the VAT is underestimated in the post scan. This results in a large VAT loss, that does not exist in reality.

6.3.1 Comparison between the old and the new method

Table 6.8 shows how many segmentation errors the new and old method make when the entire dataset is segmented. The errors are split into 4 categories according to the voxel-wise errors of the entire image series of a subject.

	% Small	Medium	Large	X-large
New Method	22	1	2	0
Old Method	22	4	3	2

Table 6.8: Segmentation errors of the new and old method.

The number of small errors are 22 for both methods. The small errors of the new method, though, seem to be systematic, when segmenting the interior SAT boundary, caused by a very specific detail on the posterior part of the abdomen, especially in the lower slices. The small errors of the old method seem to be unsystematic. A small error of both methods is shown in Figure 6.8. In Figure 6.6 a small error of the old method is also seen. The figures support the theory that the error of the old method is unsystematic as they appear different every time. A medium error is shown in Figure 6.5. If an error of this size appears in 2 or 3 slices, the error is classified as a medium error. If an error of this size appears in 4 or more than slices, it is classified large. In Figure 6.4 a large and

a X-large error of the new and old method are shown, respectively. The new method makes a mistake when segmenting the abdomen boundary. The old method both makes a mistake when segmenting the interior SAT boundary and the abdomen boundary in 4 or more slices, which classify the total error X-large. However, the mistake in the abdomen boundary is not visible in the old method because another mask, the clustering mask, is used as the background. The number of voxels indicated in top of the segmented images, are almost equal for both methods, which means that the abdomen boundary is not located correctly with the old method even though the image does not show.

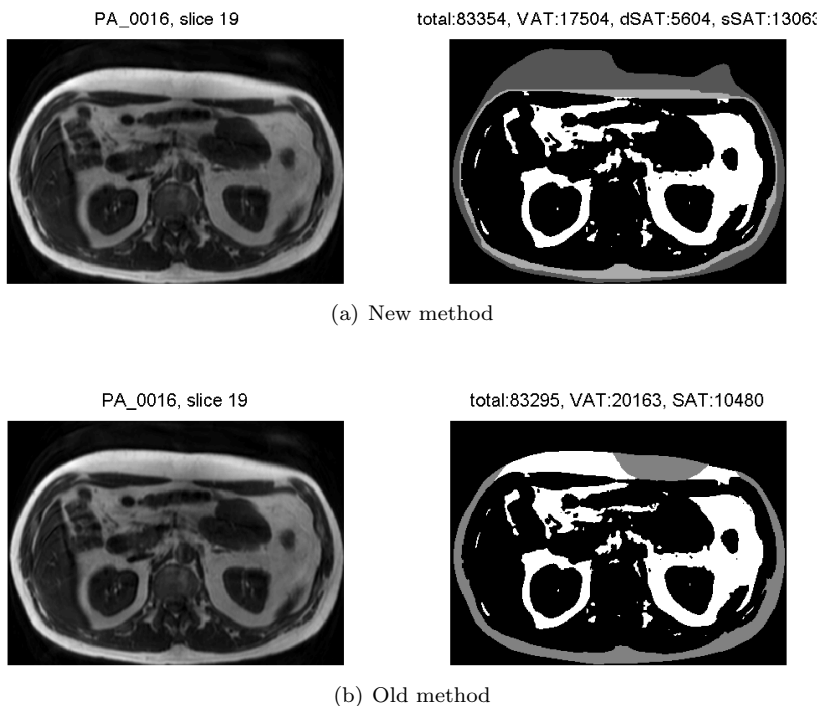


Figure 6.4: Subject 16, slice 19 segmented with the new and old method. The top image shows the error of the new method classified a large error as the abdomen boundary is not located right in 3 slices. The bottom image shows the error of the old method classified an X-large error.

The medium, large and X-large errors have been reduced from 9 with the old method to 3 with the new method. No X-large errors exist when segmenting with the new method. The medium and the two large errors of the new method

are solely due to the wrong location of the abdomen boundary using *Active Contours*. Due to this, the errors would possibly be removed, if the abdomen boundary was located using *Graph Cuts*.

6.3.1.1 Histograms

Table 6.6 shows a significant difference between the segmentation results calculated with the new and the old method. The histograms Figure 6.1, 6.2, 6.3 reveals the size of the error in the respective classes. Histogram 6.1 shows that the new method estimates the total amount of adipose tissue larger in every subject. One subject, subject 21, has an outstanding difference, 2.17%. Looking at the segmented images from subject 21, it can be seen, that both the VAT and SAT are calculated larger with the new method. However, no error in any of the algorithms have occurred. This overestimation compared to the old method, might be due to the different degrees of freedom in the bias field correction, which effects the clustering and thereby the amount of fat.

If histogram 6.3 is considered, it can be seen, that three subjects have a larger volume of VAT calculated with the old method. This is the case for subjects 47, 69 and 74. In all these subjects the location of the interior SAT boundary is not done correctly in all slices. Subject 47, slice 1, is shown in Figure 6.5, where the wrong location can be seen. This error is representative for these three outliers.

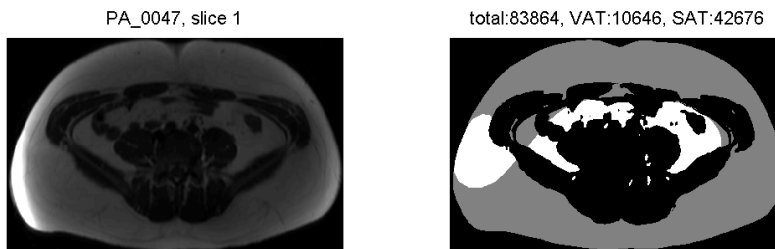


Figure 6.5: Subject 47, slice 1, segmented with the old method.

By looking at histogram 6.2 it can be seen, that 8 subjects have a larger percentage of SAT segmented with the old method. 3 subjects have a much larger percentage of SAT segmented with the new method, this is the case for subjects 46, 69, 74. There were also large differences in the VAT volume of subjects 69 and 74. Like the VAT volume, the difference is caused by a wrong segmentation

of the interior SAT boundary with the old method, this time leading to an underestimated SAT volume. Locating the interior SAT boundary is also wrong in subject 46, Figure 6.6. However, the VAT segmentation of subject 46 was not an outlier, but the difference was 0.66 %. The reason is that the segmentation of the interior SAT boundary, lead to an underestimated VAT volume inside the actual interior SAT boundary, but an overestimated VAT volume outside the boundary. This means that even though there is an error, the total VAT volume calculated is not wrong.

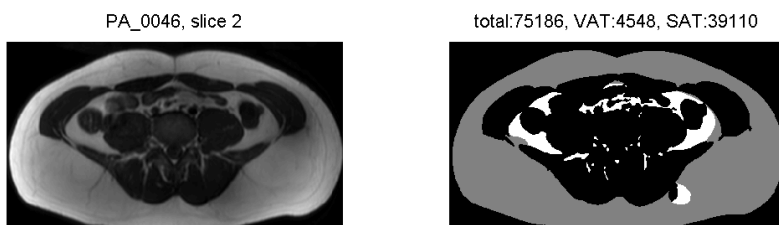


Figure 6.6: Subject 46, slice 2, segmented with the old method.

8 subjects have a larger percentage SAT-volume with the old method. This is the case for subjects 14, 26, 39, 52, 53, 55, 61, 71. In subjects 52 and 55 the percentage difference is largest, -0.59 % and -0.53 % respectively. If subject 55 is considered, it can be seen, that the interior SAT boundary is not located correctly, this time overestimating the SAT volume, Figure 6.7.

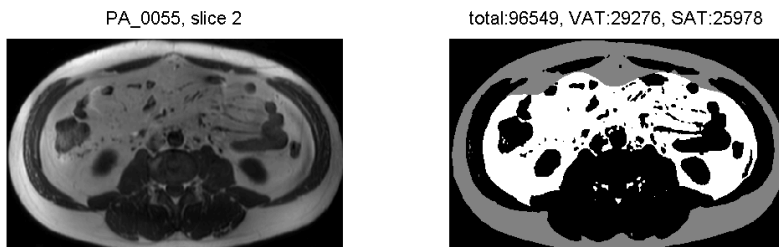


Figure 6.7: Subject 55, slice 2, segmented with the old method.

Looking at subject 52, Figure 6.8, reveals that the interior SAT boundary is located differently with the new method in both the anterior and posterior part of the image. In the posterior part, the new method makes the systematic error described in Chapter 4.4. In the anterior part the old method does not find the interior SAT correct, which overestimates the SAT volume.

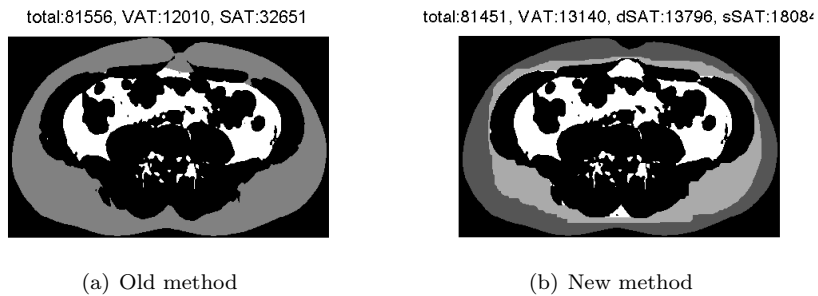


Figure 6.8: Subject 52, slice 3. Showing the segmented image with a) the old method and b) the new method.

Conclusion

The goal of this thesis was to develop an automatic method for segmentation of abdominal adipose tissue from 3-dimensional Magnetic Resonance Images. *Graph Cuts* were used to locate two boundaries, Scarpa's Fascia and the interior SAT. This was done using information in 3 dimensions. The segmentation method should be able to distinguish between 3 types of adipose tissue: visceral adipose tissue, VAT, deep subcutaneous adipose tissue, dSAT and superficial subcutaneous adipose tissue, sSAT.

The data was preprocessed before the segmentation. The abdominal boundary was located using *Active Contours*. Early in the process it was chosen to use this method, but the results in the end, unfortunately, revealed errors. To remove the *Bias Field Effect*, two methods were compared, *N3* and *Thin Plate Spline*. The *Shannon* entropy was used as a measure to evaluate the robustness of the correction methods. *Thin Plate Spline* was found to be the best method for this specific dataset.

Two methods were compared in labeling the abdomen into adipose and non-adipose tissue, *Graph Cut* and *Fuzzy C-means Clustering*. *Fuzzy C-means Clustering* was chosen. However, the *Graph Cut* method showed good potential.

Graph Cuts were used to locate the interior SAT boundary and Scarpa's Fascia, which overall seemed to give satisfying results. Combining the segmented

boundaries and the cluster labels gave the final segmentation results.

A statistical analysis was performed. From the statistics fat losses within the high and medium intensity groups compared to the control group, were observed. The analysis showed large variations in dSAT and sSAT. It is unknown whether the variations stem from the segmentation of Scarpa's Fascia or large subject variations.

Furthermore, the new and the old method were compared. The number of large errors were reduced using the new method and investigation showed that the small errors made by the new method were systematic. Histograms showing the percentage difference between the methods revealed that the new method estimated a significant larger amount of the three adipose tissue types. However, some outliers were observed. The majority of the outliers are due to the segmentation of the interior SAT boundary in the old method.

Overall the new method showed convincing results, though, there is still room for improvement.

7.1 Future work

Below is a list with possible elements for improving the segmentation results.

- Locate the abdomen boundary using *Graph Cuts*. This would possibly remove the medium and large errors of the new method shown in Table 6.8.
- Improve the method which classifies adipose tissue and non-adipose tissue. In Section 5 *Graph Cuts* seemed to be a reasonable method if the mean and variance were calculated automatic in all slices.
- Develop or use a method to make Scarpa's Fascia more visible on the images. This would result in a more accurate segmentation of the boundary.

APPENDIX A

Volume results

This section contains the distributions of abdominal adipose tissue in 12 chosen subjects, which correspond to the pre and post scanning of 6 persons. Two subjects origins from each training intensity group. The images of the segmentation for the 12 subjects are shown in Appendix B. The remaining segmentation results are included on the CD in appendix D. The adipose tissue quantity of each class is shown as a percentage of the total voxel volume. The total volume is the number of voxels in all slices in a subject inside the abdomen boundary.

A.1 Percentage of adipose tissue classes

	% FAT	% VAT	% SAT	% dSAT	% sSAT
1 - Subject 22 Pre - H	40.20%	14.69%	25.52%	10.64%	14.88%
1 - Subject 05 Post - H	37.37%	13.24%	24.14%	10.37%	13.77%
2 - Subject 53 Pre - H	46.58%	21.83%	24.75%	11.04%	13.71%
2 - Subject 63 Post - H	41.01%	18.09%	22.92%	12.17%	10.74%
3 - Subject 13 Pre - M	46.03%	19.88%	26.16%	11.05%	15.11%
3 - Subject 29 Post - M	47.26%	21.30%	25.96%	9.74%	16.22%
4 - Subject 17 Pre - M	33.82%	16.75%	17.08%	7.54%	9.54%
4 - Subject 02 Post - M	26.07%	10.38%	15.69%	74.19%	8.27%
5 - Subject 19 Pre - C	35.36%	13.47%	21.89%	10.32%	11.56%
5 - Subject 34 Post - C	36.32%	13.20%	23.12%	10.73%	12.39%
6 - Subject 43 Pre - C	35.70%	11.88%	23.82%	8.41%	15.42%
6 - Subject 74 Post - C	37.69%	11.62%	26.07%	9.52%	16.55%

A.2 Percentage weight loss

	% FAT	% VAT	% SAT	% dSAT	% sSAT
1	2.83%	1.45%	1.38%	1.11%	2.83%
2	5.57%	3.74%	1.83%	-1.13%	2.97%
3	-1.22%	-1.43%	0.20%	1.31%	-1.11%
4	7.75%	6.37%	1.39%	0.12%	1.27%
5	-0.96%	0.27%	-1.23%	-0.41%	-0.83%
6	-1.99%	0.26%	-2.25%	-1.12%	-1.13%

APPENDIX B

Segmentation results

This appendix includes the final segmentation image results of the same 6 persons contained in Appendix A. For each person the top, middle and bottom slice of the original MRI are displayed together with the corresponding segmentation result. The color coding is: white; VAT. Dark grey; sSAT. Light grey; dSAT. Black; non-adipose tissue and background. The remaining segmentation results are included on the CD in Appendix D.

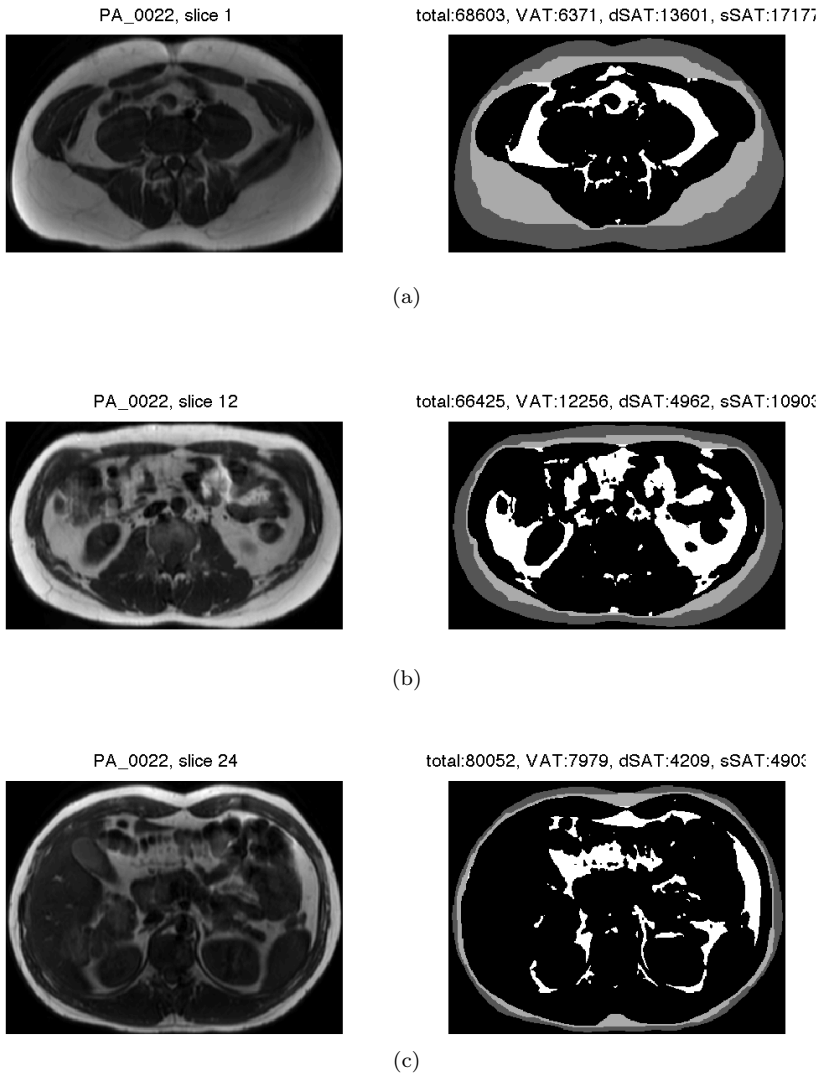


Figure B.1: Person 1. Final segmentation of subject 22. Pre-scanning. High intensity training.

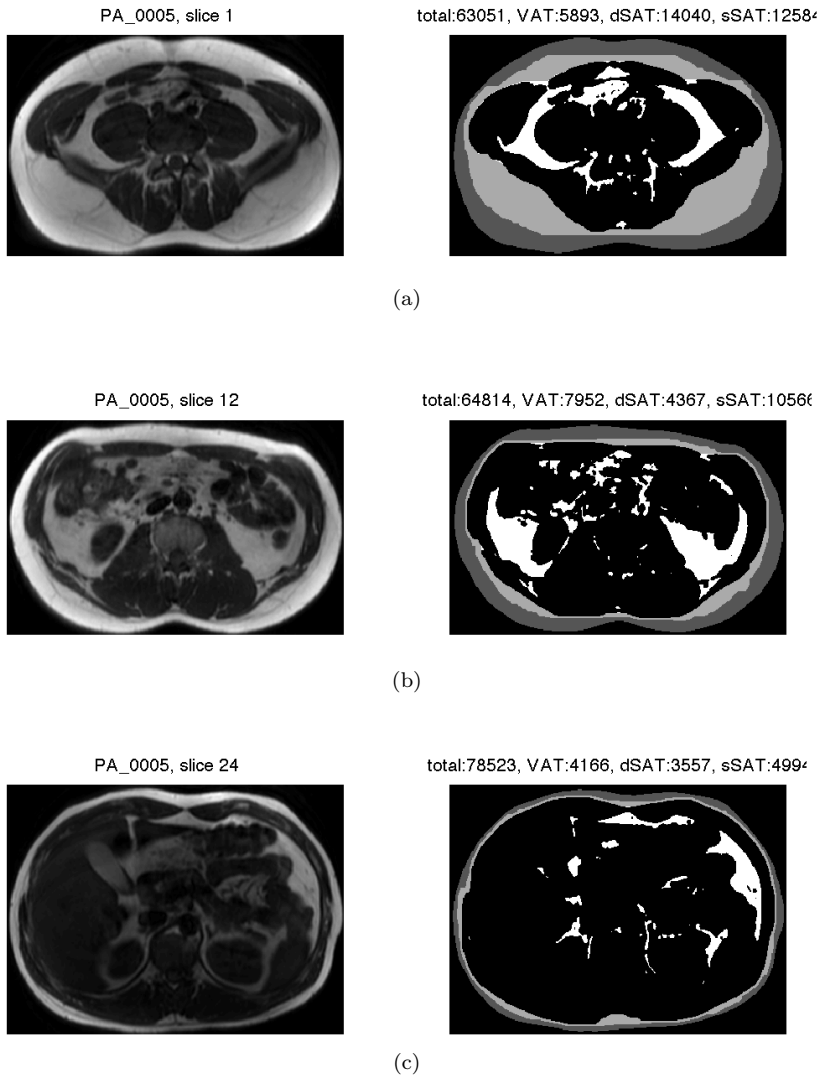


Figure B.2: Person 1. Final segmentation of subject 5. Post-scanning. High intensity training.

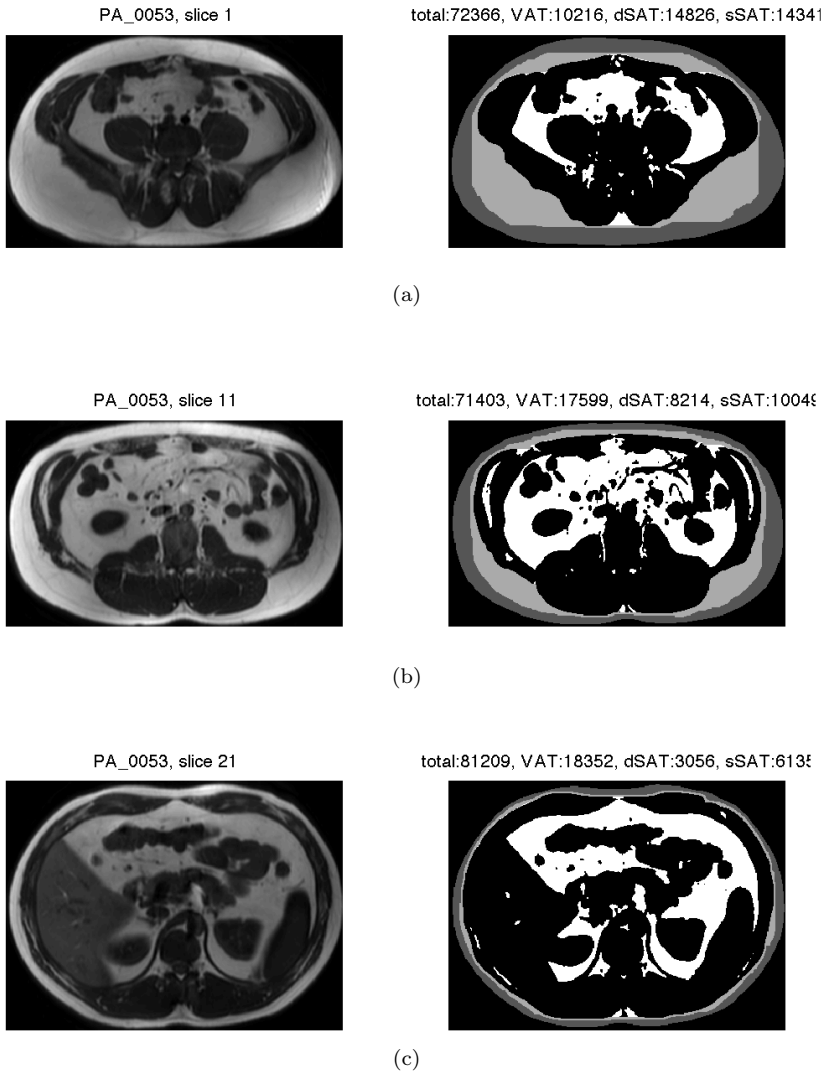


Figure B.3: Person 2. Final segmentation of subject 53. Pre-scanning. High intensity training.

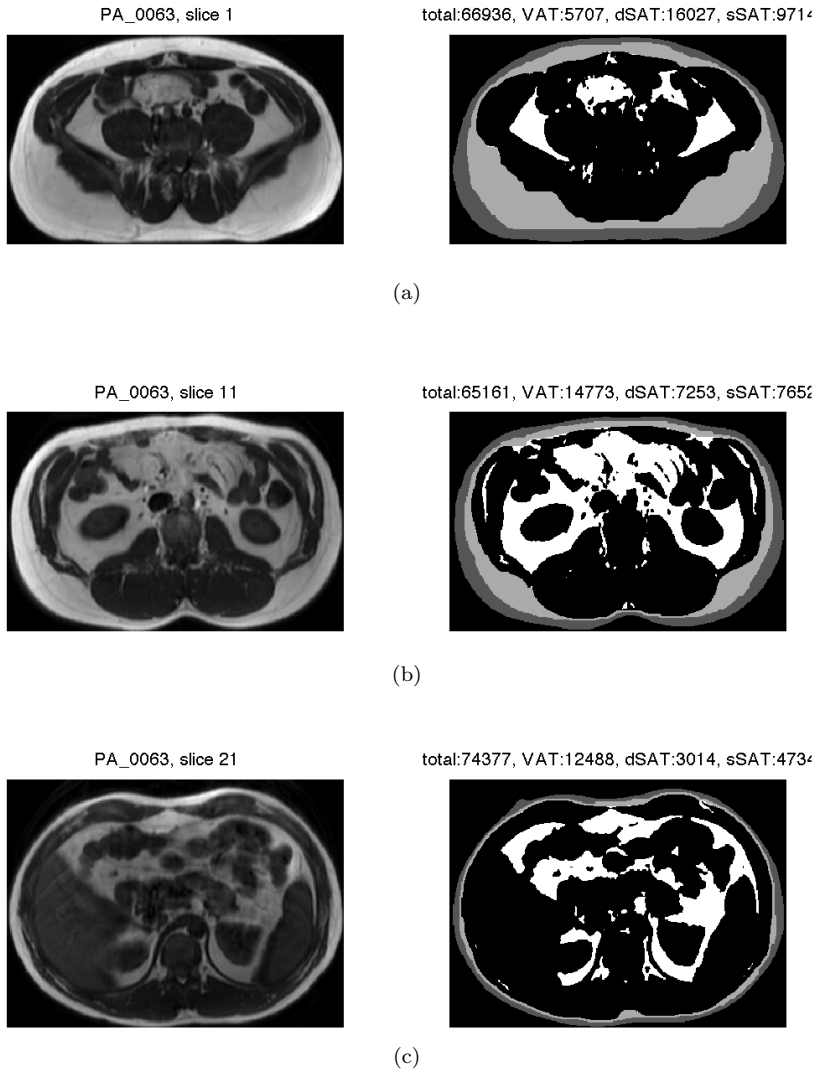


Figure B.4: Person 2. Final segmentation of subject 63. Post-scanning. High intensity training.

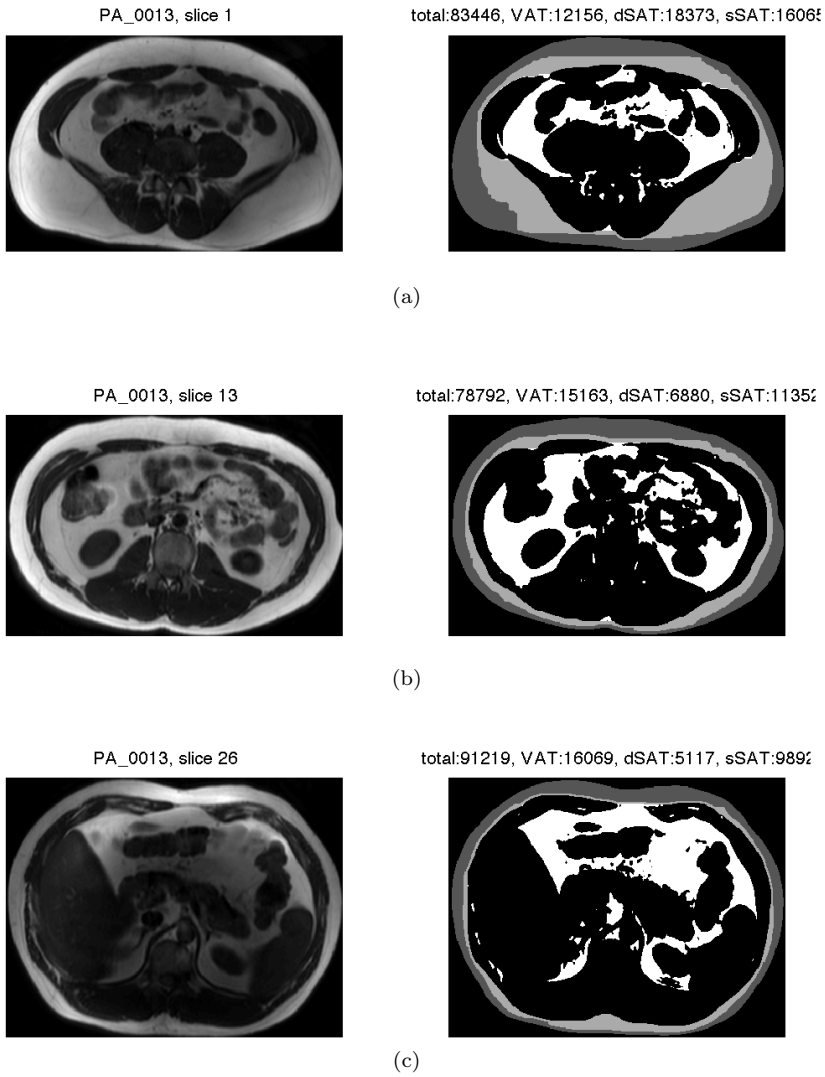


Figure B.5: Person 3. Final segmentation of subject 13. Pre-scanning. Moderate intensity training.

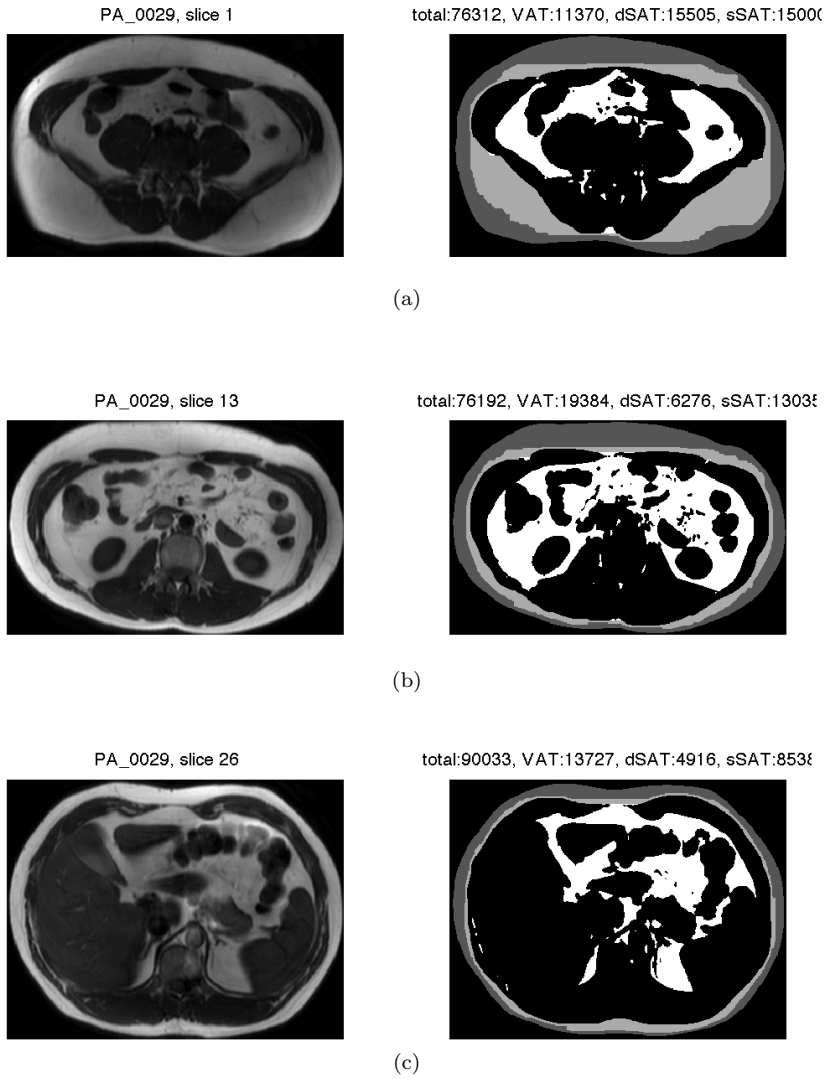


Figure B.6: Person 3. Final segmentation of subject 29. Post-scanning. Moderate intensity training.

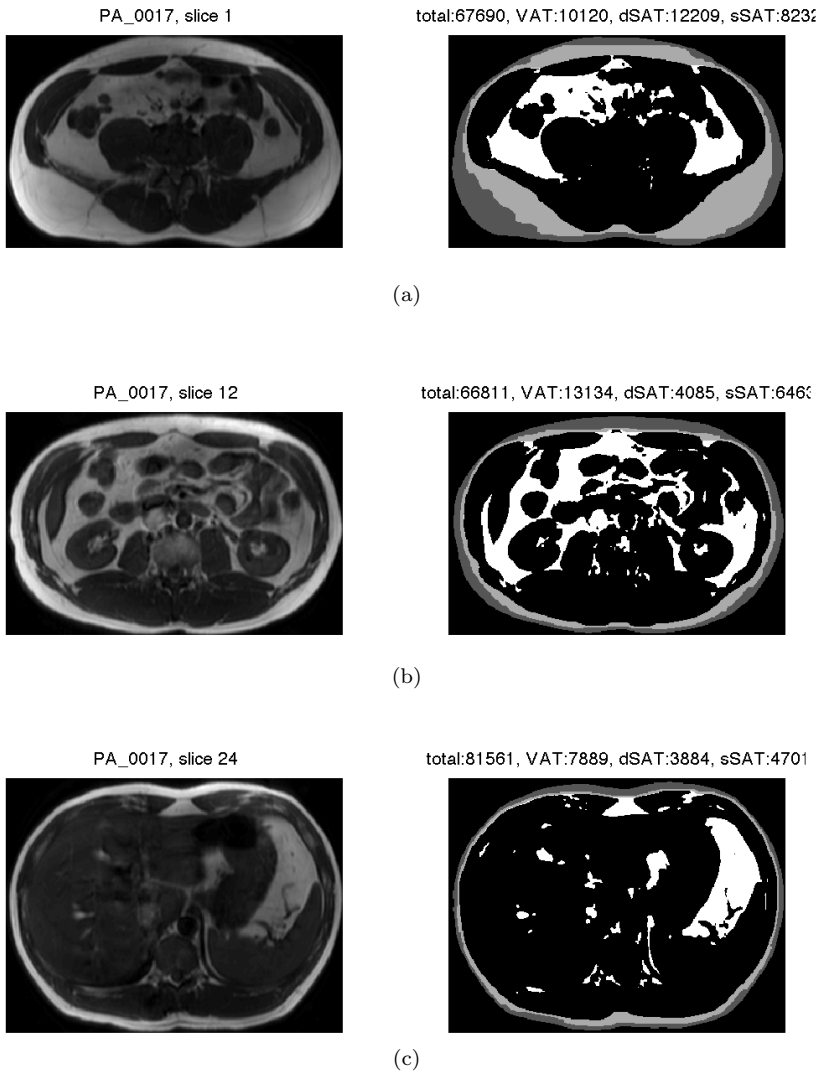


Figure B.7: Person 4. Final segmentation of subject 17. Pre-scanning. Moderate intensity training.

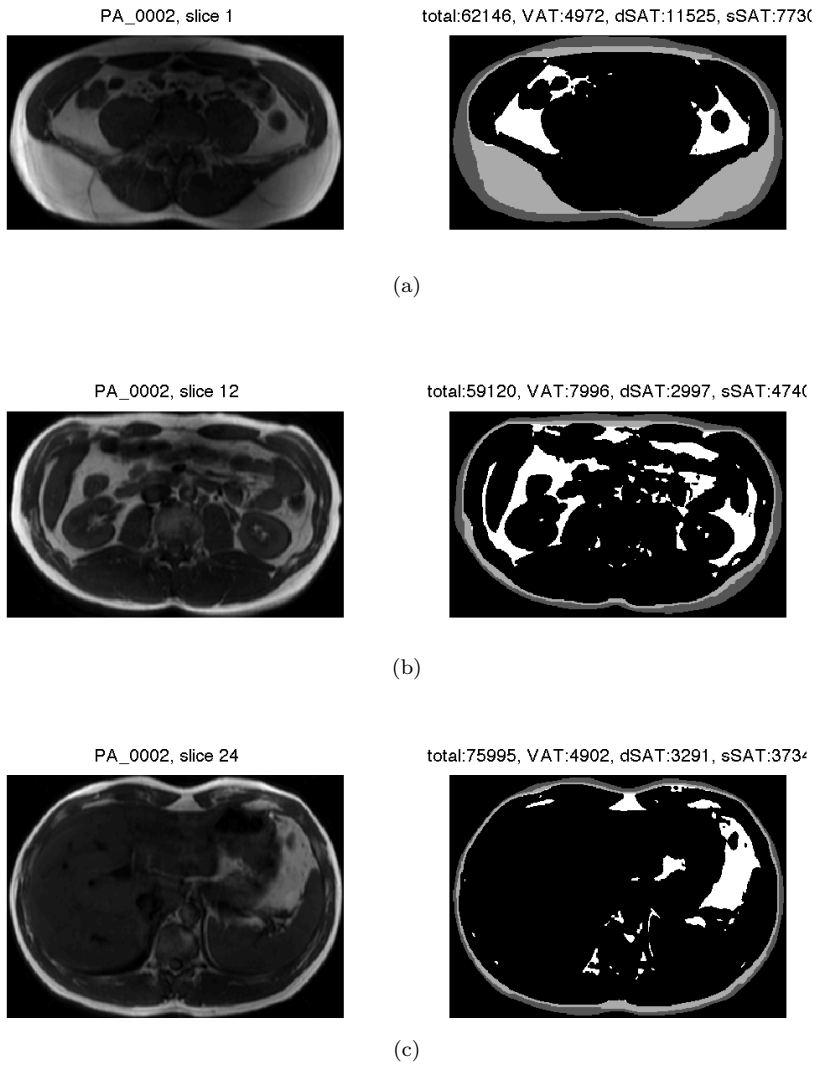


Figure B.8: Person 4. Final segmentation of subject 2. Post-scanning. Moderate intensity training.

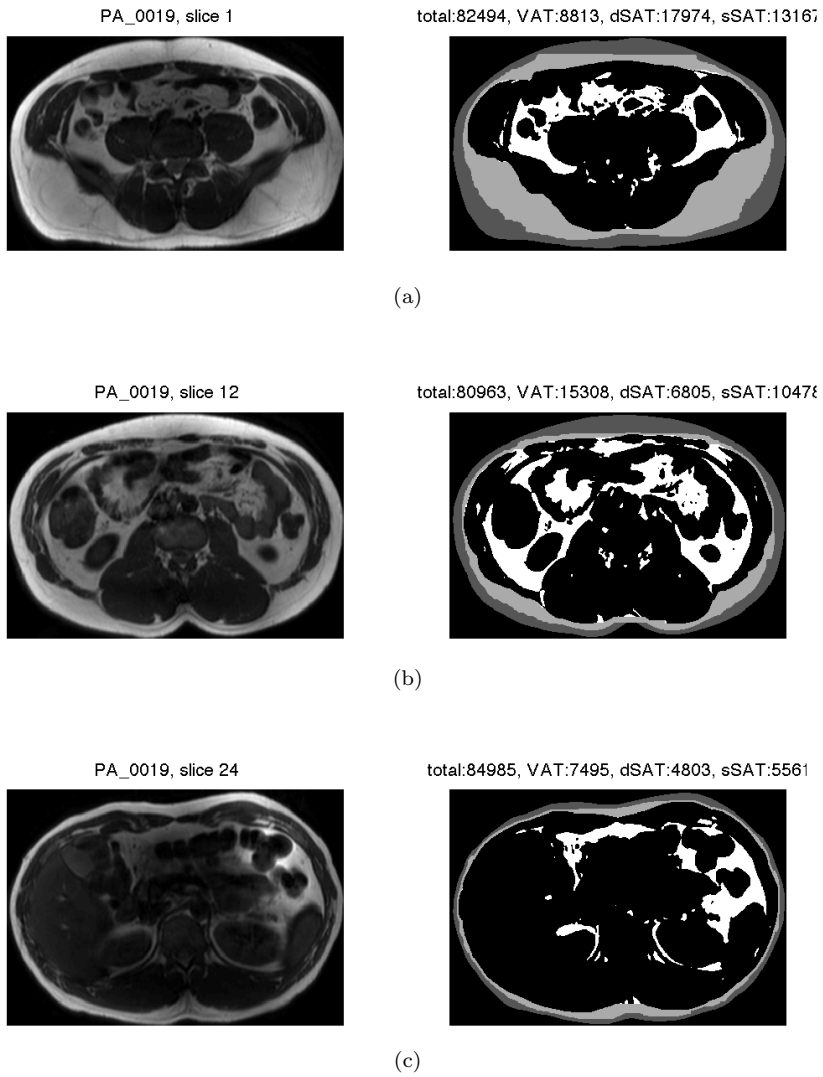


Figure B.9: Person 5. Final segmentation of subject 19. Pre-scanning. Control group.

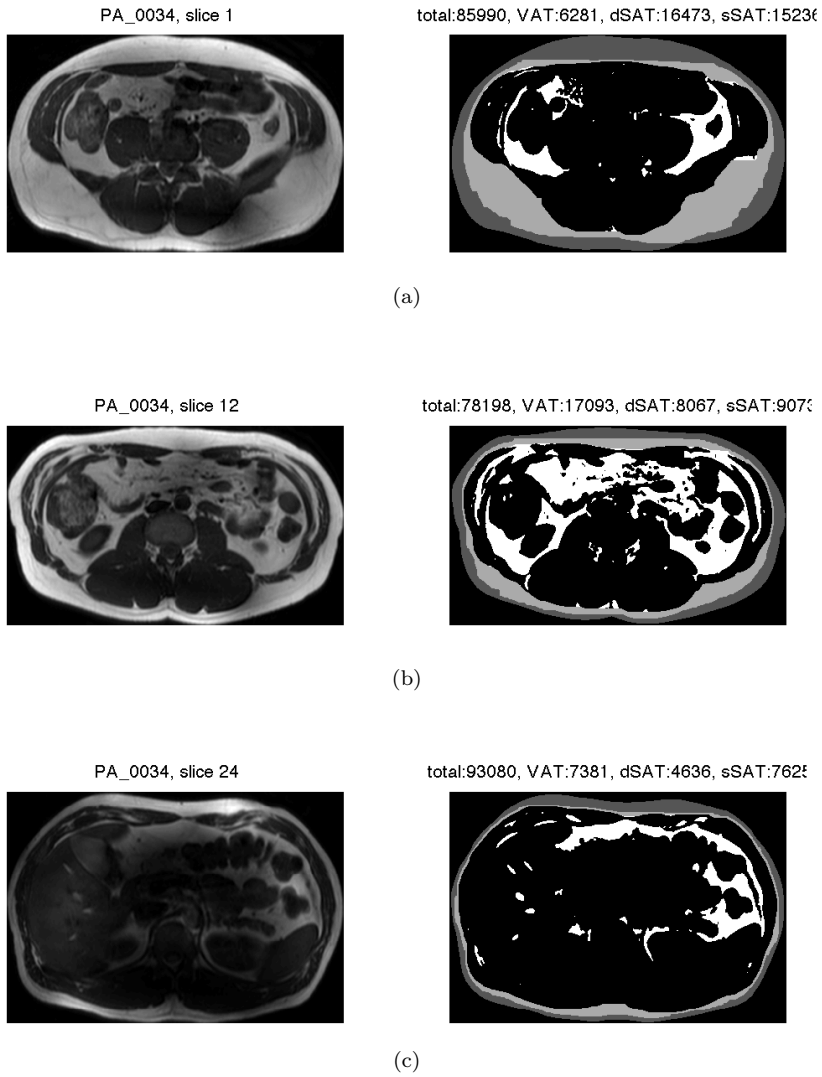


Figure B.10: Person 5. Final segmentation of subject 34. Post-scanning. Control group.

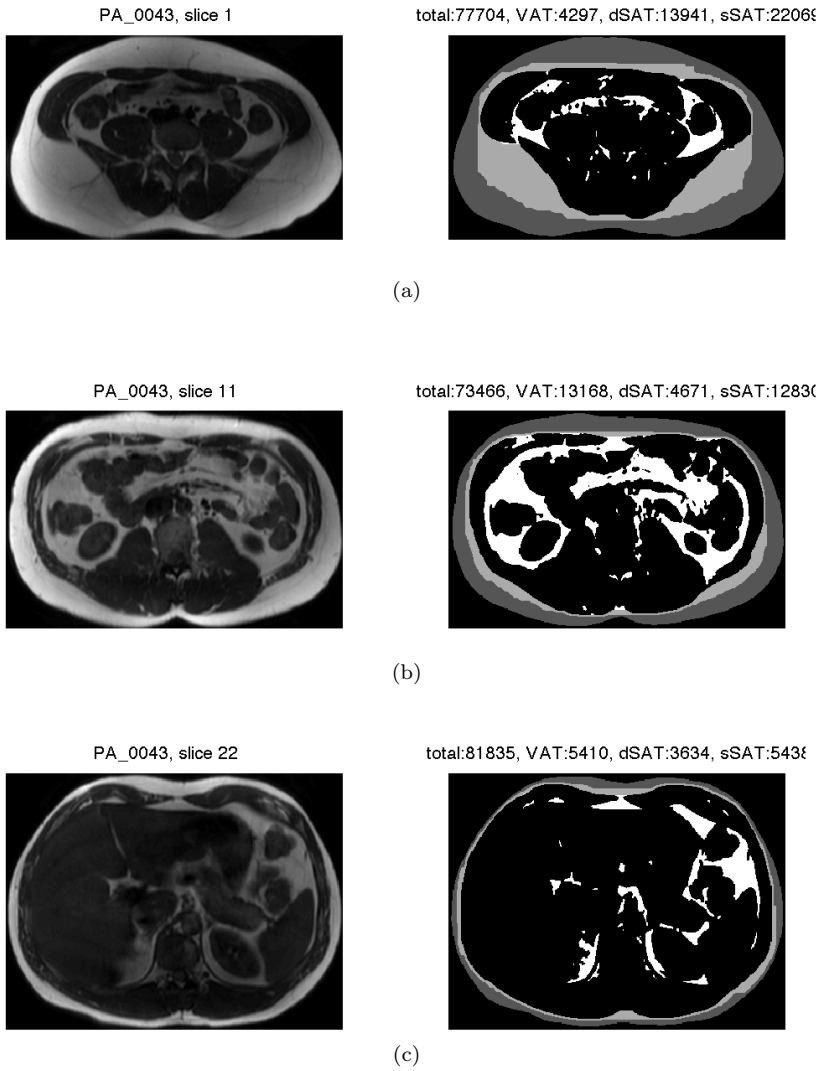


Figure B.11: Person 6. Final segmentation of subject 43. Pre-scanning. Control group.

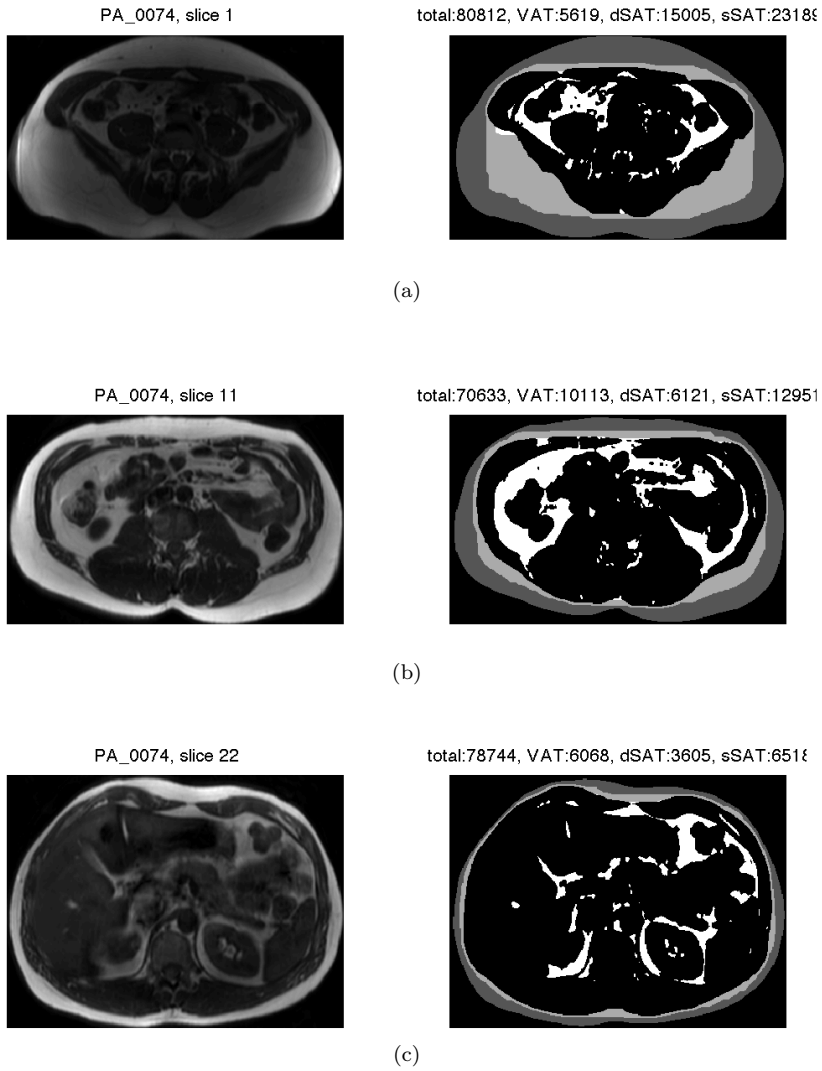


Figure B.12: Person 6. Final segmentation of subject 74. Post-scanning. Control group.

Software overview

This appendix presents a brief overview of the software developed to do the segmentation. The program consists of two main m-files. The software is implemented using MATLAB 7.9 and 7.10. To run the C++ algorithm written by Boykov and Kolmogorov [6], a C++ wrapper is used [14]. Below is a list of the most important sections (flags) of the algorithm and a short description of their functionality. All source code is available on the CD enclosed in appendix D.

mainProprocessing.m

- **doBundle** puts Dicom in a single mat-file.
- **doCorrect** performs the 3D bias field correction using a TPS.
- **doDisplay** displays original and corrected plots of the selected subject.

mainSegmentation.m

- **doCluster** cluster the regions.
- **doSegment** locating the abdomen boundary, the interior SAT boundary and Scarpa's Fascia. Classifies the abdomen into three adipose tissue classes.

- **doProcess** saving voxel information in txt-file and saving the segmented images.

doSegment includes the following important m-files:

- **getInteriorSAT.m** locates interior SAT boundary.
- **getWeights3d.m** gives the capacities of the n-links.
- **getScarpasFascia.m** locates Scarpa's Fascia.
- **getWeights3dscarpa.m** gives the capacities of the n-links.
- **doSegmentation2.m** classifies regions.

`getInteriorSAT.m`, `getWeights3d.m`, `getScarpasFascia.m` and `doSegmentation2.m` are included in Appendix E.

APPENDIX D

Data CD

The enclosed CD contains the following:

- Original and segmented images performed with the new method for all subjects.
- Original and segmented images performed with the old method for all subjects.
- List of voxel percentages of adipose tissue classes for all subjects for the new and the old method.
- The MATLAB source code and C++ algorithm.
- The R source code.

APPENDIX E

MATLAB code

E.1 M-files

E.1.1 getInteriorSAT.m

```
1 function patientstruct = getInteriorSAT(patientstruct,sd)
2 % getInteriorSAT(patienstruct,sd) locates the interiorSAT boundary.
3 %
4 %Inputs: patientstruct = patientstruct containing the biascorrected
5 %         images
6 %         sd = standard diviation
7 %
8 %Written by Josephine Jensen and Cecilie Anker
9 % 2011 - DTU - IMM
10 %%%%%%%%%%%%%%%%%%%%%%%%%%%%%%%%%%%%%%%%%%%%%%%%%%%%%%%%%%%%%%%%%%%%%%%%%
11
12 %original image
13 ori = patientstruct.imageSeriesCorrected;
14
15 % creates ellipse in the center of image
16 pixel1=ones(size(ori,1),size(ori,2));
17 pixel2=ones(size(ori,1),size(ori,2));
18
19 %center of ellipse
20 io=270; jo=256; % Standard io=270; jo=256; %Subject 63 = io =260
```

```

21 %Subject 73 = io = 290
22 %size of ellipse
23 a=40; b=130; % Standard a=40; b=130; %Subject 55 a=100; b=160;
24 for i = 1:512
25     for j = 1:512
26         if (((i-io)/a)^2+((j-jo)/b)^2)≤1
27             pixel1(i,j)=0;
28         end
29     end
30 end
31
32 %center of ellipse
33 io=280; jo=256; % standard io=280; jo=256 %Subject 63 = i0 = 270
34 %size of ellipse
35 a=65; b=140; % Standard a=65; b=140; % Subject 55 = a=110; b=150;
36 for i = 1:512
37     for j = 1:512
38         if (((i-io)/a)^2+((j-jo)/b)^2)≤1
39             pixel2(i,j)=0;
40         end
41     end
42 end
43
44
45 se = strel('square',3);
46
47 % creates ellipse all the way trough volume
48 ellipse = zeros(size(ori,1),size(ori,2),size(ori,3));
49 for n = 1:size(ori,3);
50     ellipse(:,:,1)=imerode(pixel1,se,'same');
51     ellipse(:,:,2:15)=imerode(ellipse(:,:,1:14),se,'same');
52     ellipse(:,:,16)=imerode(pixel2,se,'same');
53     ellipse(:,:,17:n)=imerode(ellipse(:,:,16:n-1),se,'same');
54 end
55
56 % % % Filtering image
57 gaussianfilter = fspecial('gaussian',[20 20],sd);
58 IM = imfilter(ori,gaussianfilter,'same');
59
60 % gradient horizontal and vertical
61 [FX FY] = gradient(IM);
62
63 % image centre
64 ctrx = size(IM,2)./2;
65 ctry = size(IM,1)./2;
66
67
68 % pixel coordinates (relative to centre)
69 for n=1:size(IM,3);
70 [X(:,:,n) Y(:,:,n)]=meshgrid([1:size(IM,1)]-ctry,[1:size(IM,2)]-ctrx);
71 end
72
73 %dotproduct
74 S = sqrt(X.*X + Y.*Y);
75 ndx = S>0;

```

```
76
77 % radial unit vector
78 X(ndx) = X(ndx) ./ S(ndx);
79 Y(ndx) = Y(ndx) ./ S(ndx);
80
81 % radial gradient
82 RG = X.*FX + Y.*FY;
83
84 % removes center of image
85 l = RG.*ellipse;
86
87 abdomen = l;
88
89 % Defines sink
90 sink = ellipse;
91 sink(sink==0)=inf;
92 sink(sink==1)=0;
93
94 % Defines source
95 source = patientstruct.exteriorMask;
96 source(source==0)=inf;
97 source(source==1)=0;
98
99
100 vNodes = (1:(size(IM,1)*size(IM,2)*size(IM,3)))';
101 vSink = sink(:);
102 vSource = source(:);
103
104 % %Node, source, sink
105 tWeights = [vNodes, vSource, vSink];
106 disp('Locating interiorSAT')
107 addpath '/Users/cecilieanker/graphCutMFH'
108
109 nNodes = size(IM,1)*size(IM,2)*size(IM,3);
110
111 Weights = getWeights3d(abdomen);
112 [Cut, Flow] = GraphCutMex(nNodes, tWeights, Weights);
113
114 % assign labels by Cut
115
116 innerSAT = zeros(size(IM,1), size(IM,2), size(IM,3));
117 innerSAT(Cut) = 1;
118
119 patientstruct.innerSAT = innerSAT;
120
121 end
```

E.1.2 getWeights3d.m

```

1 function weights=getWeights3d(img)
2 % getWeights3d(img) gets the weight of the n-links in a 3d-dataset
3 %
4 %Input  img: 3d-dataset
5 %
6 %Written by Josephine Jensen and Cecilie Anker
7 % 2011 - DTU - IMM
8 %%%%%%%%%%%%%%%%%%%%%%%%%%%%%%%%%%%%%%%%%%%%%%%%%%%%%%%%%%%%%%%%%%%%%%%%%
9
10
11 nP=numel(img);
12
13 b = img(:);
14
15 %create matrices that has increasing numbers downwards and leftwards
16 A=img;
17 A(:)=1:nP;
18 B=A;
19 C=A;
20
21 % %shift to find neighbour correspondance
22 A_shift=circshift(A,[0 0 1]);
23 B_shift=circshift(B,[0 1 0]);
24 C_shift=circshift(C,[1 0 0]);
25
26
27 %remove column that wraps around after shifting
28 A=A(:, :, 2:end);
29 A_shift=A_shift(:, :, 2:end);
30
31 %remove row that wraps around after shifting
32 B=B(:, 2:end, :);
33 B_shift=B_shift(:, 2:end, :);
34
35 %remove column that wraps around after shifting
36 C=C(2:end, :, :);
37 C_shift=C_shift(2:end, :, :);
38
39
40 weights=[A(:), A_shift(:),
41          (ones(size(A(:))) ./150, (ones(size(A_shift(:)))) ./150; %depth
42          B(:), B_shift(:),
43          (max(b)-b(B(:))), (max(b)-b(B_shift(:))); % Vertical
44          C(:), C_shift(:),
45          (max(b)-b(C(:))), (max(b)-b(C_shift(:)))];% horizontal
46 end

```


E.1.3 getScarpasFascia.m

```

1 function patientstruct = getScarpasFascia(patientstruct)
2 % getScarpasFascia(patientstruct) locates the Scarpa's Fascia.
3 %
4 %Inputs: patientstruct = patientstruct containing the biascorrected
5 %         images and the interior SAT boundary
6 %
7 %
8 %Written by Josephine Jensen and Cecilie Anker
9 % 2011 - DTU - IMM
10 %%%%%%%%%%%%%%%%%%%%%%%%%%%%%%%%%%%%%%%%%%%%%%%%%%%%%%%%%%%%%%%%%%%%%%%%%
11
12 IM = patientstruct.imageSeriesCorrected;
13
14 %IM=patientstruct.imageSeries;
15
16 % image centre
17 ctrx = size(IM,2)./2;
18 ctry = size(IM,1)./2;
19
20 % gradient
21 [FX FY] = gradient(IM);
22
23 for n=1:size(IM,3);
24 % pixel coordinates (relative to centre
25 [X(:, :, n) Y(:, :, n)]=meshgrid([1:size(IM,1)]-ctry, [1:size(IM,2)]-ctrx);
26 end
27
28 S = sqrt(X.*X + Y.*Y);
29 ndx = S>0;
30
31 % radial unit vector
32 X(ndx) = X(ndx)./S(ndx);
33 Y(ndx) = Y(ndx)./S(ndx);
34
35 % radial gradient
36 RG = X.*FX + Y.*FY;
37
38 %Laplace
39 [FX2 FY2]= gradient(RG);
40
41
42 RG2 = X.*FX2 + Y.*FY2;
43
44 %makes outer mask smaller and inner mask bigger.
45
46 se = strel('square',3);
47
48 outer=imerode(patientstruct.mask,se,'same');
49 outer=imerode(outer,se,'same');
50 outer=imerode(outer,se,'same');
51 outer=imerode(outer,se,'same');

```

```

52
53 inner=imerode(patientstruct.innerSAT,se,'same');
54 inner=imerode(inner,se,'same');
55
56 abdomen=RG2.*inner.*outer;
57
58 %defines sink
59 sink = inner;
60 sink(sink==0)=inf;
61 sink(sink==1)=0;
62
63 %defines source
64 source = outer;
65 source(source==0)=inf;
66 source(source==1)=0;
67
68
69 vNodes = (1:(size(IM,1)*size(IM,2)*size(IM,3)))';
70 vSink = sink(:);
71 vSource = source(:);
72
73 % %Node,source,sink
74 tWeights =[vNodes,vSink, vSource];
75 disp('Locating Scarpas Fascia')
76 addpath '/Users/cecilieanker/graphCutMFH'
77
78 nNodes=size(IM,1)*size(IM,2)*size(IM,3);
79
80 Weights=getWeights3dscarpa(abdomen);
81 [Cut,Flow] = GraphCutMex(nNodes,tWeights,Weights);
82
83 % assign labels by Cut
84
85 scarpa = zeros(size(IM,1),size(IM,2),size(IM,3));
86 scarpa(Cut)=1;
87
88 patientstruct.scarpa=scarpa;
89 end

```

E.1.4 doSegmentation2.m

```

1 function patientstruct=doSegmentation2(patientstruct)
2
3 doPlots = 0;
4
5
6 %Makes x-y points of the segmented boundaries
7 for n=1:size(patientstruct.imageSeriesCorrected,3);
8
9 %innerSAT

```

```
10 innerSATXY(:,:,n)=bwboundaries(patientstruct.innerSAT(:,:,n));
11 patientstruct.innerSATXY = innerSATXY;
12 %Scarpas Fascia
13 scarpasXY(:,:,n)=bwboundaries(patientstruct.scarpa(:,:,n));
14 patientstruct.scarpasXY = scarpasXY;
15 %outer abdomen
16 outerSATXY(:,:,n)=bwboundaries(patientstruct.exteriorMask(:,:,n));
17 patientstruct.outerSATXY = outerSATXY;
18
19 end
20
21 % Classifies the different adipose tissue classes
22 SAT=patientstruct.exteriorMask.*patientstruct.innerSAT;
23
24 SAT2=1-SAT;
25
26 VAT=SAT2.*patientstruct.clusterLabels.*patientstruct.exteriorMask;
27
28 scarpa2 = 1 - patientstruct.scarpa;
29 sSAT=patientstruct.exteriorMask.*scarpa2;
30
31 dSAT=patientstruct.scarpa.*patientstruct.innerSAT;
32
33 classes = 3*VAT + 2*dSAT + 1*sSAT;
34
35 %save relevant types of addipose tissue
36
37 patientstruct.SAT=SAT;
38 patientstruct.VAT=VAT;
39 patientstruct.dSAT=dSAT;
40 patientstruct.sSAT =sSAT;
41 patientstruct.classes=classes;
42
43 % Plots the results
44 if doPlots
45
46
47 % slice number
48 for u=1:size(patientstruct.imageSeriesCorrected,3);
49
50 %semented images
51 figure;
52 imagesc(classes(:,:,u));
53 colormap gray
54 axis square
55 axis off
56
57 end
58
59 end
```


Statistical analysis in R

F.1 R-code

```
#intensity groups and fat type
h_fat=c(almafat,anapfat,brfrfat,grpefat,minifat,dejefat,hejefat,jakufat,mimrfat,nihafat)
m_fat=c(casofat,deknfat,jechfat,stmofat,ulrafat,lapifat,lespfat,odrufat,peknfat,hahofat)
c_fat=c(anbrfat,ankrfat,anmofat,henifat,krmnfat,mavefat,peerfat,erhofat)

#Bartlett's test
fat=c
(almafat,anapfat,brfrfat,grpefat,minifat,dejefat,hejefat,jakufat,mimrfat,nihafat,casofat,deknfat,jechf
at,stmofat,ulrafat,lapifat,lespfat,odrufat,peknfat,hahofat,anbrfat,ankrfat,anmofat,henifat,krmnfat,mav
efat,peerfat,erhofat)
g=factor(c(1,1,1,1,1,1,1,1,1,2,2,2,2,2,2,2,2,2,2,3,3,3,3,3,3,3))
bartlett.test(fat,g)

#test of nullhypothesis that  $\mu_0=\mu_1=\mu_2=\mu_3$ 
anova(lm(fat~g))
```

Figure F.1: R-code. Bartlett's test and ANOVA test between intensity groups and fat type. The code is shown for total fat. A similar code exists for SAT and VAT.

```
#Unpaired t-test
t.test(h_fat,m_fat,conf.level=0.99,var.equal=TRUE)
t.test(h_fat,c_fat,conf.level=0.99,var.equal=TRUE)
t.test(m_fat,c_fat,conf.level=0.99,var.equal=TRUE)

t.test(h_sat,m_sat,conf.level=0.99,var.equal=TRUE)
t.test(h_sat,c_sat,conf.level=0.99,var.equal=TRUE)
t.test(m_sat,c_sat,conf.level=0.99,var.equal=TRUE)

t.test(h_vat,m_vat,conf.level=0.99,var.equal=TRUE)
t.test(h_vat,c_vat,conf.level=0.99,var.equal=TRUE)
t.test(m_vat,c_vat,conf.level=0.99,var.equal=TRUE)
```

Figure F.2: R-code. Unpaired t-tests between intensity groups and adipose tissue type.

Bibliography

- [1] Henrik Aanæs. Graph cuts for markov random fields (mrf). *DTU, IMM*, January 2011.
- [2] M. N. Ahmed, Sameh M. Yamany, Nevin Mohamed, Aly A. Farag, and Thomas Moriarty. A modified fuzzy c-means algorithm for bias field estimation and segmentation of mri data A. *IEEE Transactions on medical imaging*, 21:193–199, March 2002.
- [3] Yuri Boykov and Gareth Funka-Lea. Graph cuts and efficient n-d image segmentation. *International Journal of Computer Vision*, 26:109–131, 2006.
- [4] Yuri Boykov and Marie-Pierre Jolly. Interactive organ segmentation using graph cuts. *MICCAI*, pages 276–286, October 2000.
- [5] Yuri Boykov and Marie-Pierre Jolly. Interactive graph cuts for optimal & region segmentation of objects in n-d. *International Conference on Computer Vision*, 1:105–112, July 2001.
- [6] Yuri Boykov and Vladimir Kolmogorov. An experimental comparison of min-cut / max-flow algorithms for energy minimization in vision. *IEEE Transactions on pattern analysis and machine intelligence*, 26:1124–1137, September 2004.
- [7] Lotte H. Enevoldsen, Lene Simonsen, Bente Stallkhecht, Henrik Galbo, and Jens Bulow. In vivo human lipolytic activity in preperitoneal and subdivisions of subcutaneous abdominal adipose tissue. *The American Physiological Society*, 0193-1849/01:E1110–E1114.

-
- [8] Rasmus Engholm, Aleksandr Dubinskiy, Rasmus Larsen, Lars G. Hansen, and Berit Ostergaard Christoffersen. An adipose segmentation and quantification scheme for intra abdominal region on minipigs. *Medical Imaging 2006: Image Processing*, 6144:61443U–1.
- [9] E. Kelley et al. Subdivisions of subcutaneous abdominal adipose tissue and insulin resistance A. *Am J Physiol Endocrinol Metab*, 278:E941–E948, 2000.
- [10] Kang Li et al. Optimal surface segmentation in volumetric images - a graph-theoretic approach A. *IEEE Transactions on pattern analysis and machine intelligence*, 28(1):119–134, January 2006.
- [11] Slices from course 02503. Markov random fields. *DTU, IMM*.
- [12] <http://fine.ku.dk/>.
- [13] <http://surfer.nmr.mgh.harvard.edu/>.
- [14] <http://www.adastral.ucl.ac.uk/vladkolm/software.html>.
- [15] Qing Ji, John O. Glass, and Wilburn E. Reddick. A novel, fast entropy-minimization algorithm for bias field correction in mr images. *Magnetic Resonance Imaging*, 25:259–264.
- [16] Kang Li, Xiaodong Wu, Danny Z. Chen, and Milan Sonka. Efficient optimal surface detection: Theory, implementation and experimental validation. *Proc. SPIE Int'l Symp. Medical Imaging: Image Processing*, 5370:620–627, May 2004.
- [17] Thomas Hammershaimb Mosbech. Fat segmentation in abdominal mr-scans. *Master Thesis. DTU, IMM*, 2008.
- [18] Thomas Hammershaimb Mosbech, Kasper Pilgaard, Rasmus Larsen, and Allan Vaag. Automatic segmentation of abdominal adipose tissue in up-percaseMRI. In Anders Heyden and Fredrik Kahl, editors, *Proceedings of the 17th Scandinavian Conference on Image Analysis*, Lecture Notes in Computer Science, Springer, May 2011.
- [19] Martin Bæk Petersen. Variation in liver lipids in young overweight males - dose-response effects of exercise. *Master thesis. Unpublished*, 2011.
- [20] John G. Sled, Alex P. Zijdenbos, and Allen C. Evans. A nonparametric method for automatic correction of intensity nonuniformity in mri data. *IEEE Transactions on Medical Imaging*, 17:87–97.

-
- [21] Steven R. Smith, Jennifer C. Lovejoy, Frank Greenway, Donna Ryan, Lillian deJonge, Jacques de la Bretonne, Julia Volafova, and George A. Bray. Contributions of total body fat, abdominal subcutaneous adipose tissue compartments, and visceral adipose tissue to the metabolic complications of obesity. *The American Physiological Society*, 50:425–435.